

ABSTRACT

Title of thesis: OPTICAL PROPERTIES OF STRESSED SILICON NITRIDE FILMS AND THEIR IMPACT ON HIGH CONTRAST GRATING PERFORMANCE

Navin Lingaraju, Master of Science, 2017

Thesis directed by: Dr. John Lawall
National Institute of Standards and
Technology (NIST)

In cavity-based optomechanical platforms, the coupling between the optical modes of a cavity and the vibrational modes of a mechanical resonator is mediated by radiation pressure. High contrast gratings (HCGs) have attracted a lot of interest for such platforms because they offer a way to make high reflectivity ($> 99.5\%$), low mass mirrors. In its simplest form, a high contrast grating is a high index dielectric slab that has been patterned with sub-wavelength scale features to create a periodic modulation of the refractive index in one or two dimensions. Optomechanical platforms also need these low mass reflectors to act as mechanical resonators with a high mechanical quality factor Q . Stressed silicon nitride on silicon has emerged as a leading candidate for such devices because these films possess mechanical quality factors in excess of 10^5 . Due to the stress that these silicon nitride films are under, 2D HCGs end up being more tolerant of the microfabrication process than their 1D counterparts. Additionally, those based on a symmetric 2D photonic crystal lattice are

expected to be insensitive to the polarization of light at normal incidence. This thesis looks at the performance of 2D silicon nitride HCGs, as well as examines some of the properties of stressed silicon nitride films that limit their performance. We present a new method to separate transmission losses from dissipative losses in an HCG and find that dissipative losses are not the dominant factor in limiting the reflectivity of 2D HCGs. Our results also show that a slight anisotropy in the refractive index of stressed silicon nitride films can make these HCGs birefringent, thereby breaking the degeneracy between polarization eigenmodes when the HCGs are used as the end mirror in an optical cavity.

OPTICAL PROPERTIES OF STRSSED SILICON NITRIDE
FILMS AND THEIR IMPACT ON HIGH CONTRAST
GRATING PERFORMANCE

by

Navin Bhartoor Lingaraju

Thesis submitted to the Faculty of the Graduate School of the
University of Maryland, College Park in partial fulfillment
of the requirements for the degree of
Master of Science
2017

Advisory Committee:
Professor Jeremy Munday, Chair/Advisor
Dr. John Lawall, Co-Advisor
Professor Mohammad Hafezi

©Copyright by
Navin Bhartoor Lingaraju
2017

For my family

Acknowledgements

I would like to take a moment to acknowledge the many people who have supported me in this endeavor. I am especially grateful to my colleagues at the National Institute of Standards and Technology for their guidance during this project. In particular, I want to thank Dr. Yichen Shuai, who fabricated the high contrast gratings used in my research. Thank you for also training me to fabricate these devices, as well as sharing your many insights on the process. I am also grateful to Dr. Justin Foley, whose wealth of knowledge about guided mode resonance filters has improved my understanding of the subject. Above all, I would like thank my mentor, Dr. John Lawall, from whom I have learned so much in such a short period of time. Thank you for your guidance, patience, and kindness over the last couple of years. Any success I have in the future I will owe in large part to your mentorship. I want thank the members of my committee for their service and feedback during this process. I would be remiss if I did not take special note of the role my academic advisor, Professor Jeremy Munday, played in keeping my graduate career on track. Thank you for keeping my eye on the big picture and helping me understand how to tailor my graduate education to set up the next steps in my career.

Finally, I would like to thank my family for their unwavering support. I owe a great deal to my parents and my brother, who have all been understanding of the long absences between my visits home. Most of all, I want to thank my wife Laura for her love and support. This would not have been possible without you.

Table of Contents

List of Figures	vi
List of Publications	x
1 Introduction	1
1.1 Cavity Optomechanics and HCGs	2
1.2 Optical Properties of Silicon Nitride and Impact on HCG Performance	4
1.3 Goals and Objectives	6
1.4 Outline of Thesis	7
2 Determination of Reflectivity, Transmittance, and Loss	9
2.1 Determining Mirror Reflectivity from Cavity Finesse Measurements	10
2.2 Cavity Transmission and Cavity Reflection Signals	12
2.3 Practical Limits and Considerations	15
2.4 Cavity Configurations	16
2.4.1 HCG Input Coupler	17
2.4.2 HCG Output Coupler	18
2.5 Summary	19
3 Measurement of HCG Performance	20
3.1 HCG Fabrication	20
3.2 Cavity Experiments	21
3.3 HCG Reflectivity	24
3.4 Nondegenerate Polarization Eigenmodes	26
3.5 Short Cavity with HCG Output Coupler	30
3.5.1 HCG Reflectivity	30
3.5.2 Properties of Polarization Eigenmodes	32
3.5.3 “Anomalous Peak”	34
3.6 Separation of HCG Transmittance from Scattering and Absorption Loss	35
3.7 Summary	37
4 Effect of Index Anisotropy and Dissipative Loss	39
4.1 Anisotropic Refractive Index in Stressed Silicon Nitride	39
4.1.1 Toy Model HCG	39
4.1.2 RCWA Simulations	44
4.2 Separation of Absorption from Scattering	50
4.2.1 Effect of Absorption Loss on HCG Reflectivity	51
4.2.2 Estimate of Scattering Losses	53
4.3 Summary	56

5	Conclusions and Future Work	58
5.1	Conclusions	58
5.2	Future Work	60
5.2.1	Design and Fabrication	60
5.2.2	Metrology	61
5.2.3	Optomechanics	61
Appendix A: Relating mirror parameters to the transmitted and re- flected signals		63
Bibliography		72

List of Figures

1	The reflective membrane in Fabry-Pérot cavity can be modeled as a mirror on a spring.	2
2	Illustration of a 1D and a 2D high contrast grating.	3
3	The force exerted by radiation pressure on the end mirrors of a laser cavity depends on the round trip gain profile of the laser. When an HCG with a high optical Q is used as one of the end mirrors, the round trip gain profile is defined, almost entirely, by the spectral response of the HCG. The graph above shows how the force on a high Q reflector changes with the length of the laser cavity. If the cavity length is tuned to ensure that the oscillating mode is blue-detuned, the HCG sweeps out a path similar to the one depicted above.	5
4	(left) Fabry-Pérot cavity showing light incident from the left and exiting the through the flat mirror as the cavity transmission signal. (right) Cavity transmission as a function frequency ν_{opt}	10
5	A hemispherical Fabry-Pérot resonator. The net signal propagating from the input face of the first mirror is cavity reflection signal (R_{cavity}). The cavity transmission signal is denoted by T_{cavity}	11
6	Excerpt of experimental data showing the change in R_{cavity} and T_{cavity} as a function of wavelength.	13
7	Alternate configurations for cavity measurements	17
8	(left) SEM images showing the photonic crystal pattern inscribed within a circular region of the membrane. (right) Close up of a few unit cells of the lattice.	21
9	Setup of cavity experiment used to determine the reflectivity of HCGs.	22
10	The second EO phase modulator generates two sidebands, which are offset by 10MHz from the carrier. The sideband-sideband spacing of 20Mz is used to convert the bottom axis of the oscilloscope trade from one of time to one of frequency. Based on this frequency reference, the linewidth of the carrier above estimated to be 890kHz full width at half maximum (FWHM).	24
11	(left) Calculated coefficients of finesse over wavelengths from 1550nm-1560nm. (right) Corresponding cavity resonance linewidths.	25
12	(left) Calculated HCG reflectivity over the wavelengths from 1550nm-1560nm. (right) Comparison between cavity experiments (R_{HCG}) and simple transmission measurements ($1 - T_{HCG}$).	26
13	(top) Cavity transmission signals measured at various wavelengths. (bottom) Frequency offset between closely spaced cavity resonances as a function of wavelength.	27

14	Oscilloscope trace of the cavity transmission signal when circularly polarized light is incident on the cavity. The insets show the transverse profile of the transmitted beam when the laser was locked to the corresponding peak.	28
15	The cavity was locked to each of two closely spaced cavity resonances. The power in the transmitted signal was analyzed in increments of 10 degrees using a polarizer and the results recorded on a polar plot. . .	29
16	(left) Normalized cavity transmission signal over the wavelength range from 1520nm - 1600nm. (right) Raw cavity transmission and reflection signals around 1556nm, the region of highest reflectivity.	31
17	(left) Cavity finesse as a function of wavelength for both polarization eigenmodes. (right) Inferred HCG reflectivity over the range from 1553nm - 1563nm.	31
18	Difference in phase shift imparted by the HCG to the eigenmodes based on data from both the long ($L_{cavity} = 49.5mm$) and short cavity ($L_{cavity} = 0.42mm$)	33
19	Orientation of the linearly polarized eigenmodes relative to the horizontal and vertical axes.	34
20	Normalized transmission of a focused beam through the 2D HCG. When this HCG is used as the end mirror in a Fabry-Pérot cavity, the coefficient of finesse drops below 100 for values of transmission over 6%.	35
21	(left) R_{min} and T_{max} for the near vertical polarization eigenmode. (right) Possible solutions for $T_{dielectric}$. (NOTE: Optical losses (transmission + absorption + scattering) from the dielectric mirror are known to be $\cong 0.00015$.)	36
22	Optical losses from the HCG are separated into HCG transmittance and a lumped quantity that captures the total scattering and absorption loss.	37
23	Cavity where the HCG is modeled as a compound element consisting of a perfectly transmitting wave retarder and a high reflectivity mirror.	40
24	Plot of the calculated cavity transmission signal using the dielectric mirror reflectivity of 0.99984 and cavity length $L_{cavity} = 0.4mm$. As an example, incident light was assumed to be linearly polarized and oriented at 60° from the x-axis. For illustration purposes, a smaller “HCG reflectivity” (0.99 vs. 0.999 actual) and larger differential phase shift (0.4 vs. 0.02 actual) from the wave retarder were used in calculations.	42
25	Similar to the plot in figure 24, but over a few FSR.	43
26	Model showing the relevant parameters used in simulations.	45

27	Graph of the difference in orientation between the electric field vector of the incident field ($\tan^{-1}(\frac{E_{y_{inc}}}{E_{x_{inc}}})$) and that of the total field ($\tan^{-1}(\frac{E_{y_{tot}}}{E_{x_{tot}}})$). The electric field was calculated for situations where an incident plane wave starts out at $z = 0\mu m$, propagates to the right, and encounters an HCG placed at $z = 20\mu m$. Green signifies regions where the orientation of the electric field vectors are nearly the same for both the incident ($E_{incident}$) and the total field ($E_{incident} + E_{reflected}$).	46
28	(a), (b) Magnitude of the electric field for the reflected waves, which propagate from right to left after encountering the HCG placed at $z = 20\mu m$. (c) Traces from (a) and (b) for $x = 0\mu m$	47
29	Comparison between the experimentally measured difference in phase shift imparted to orthogonal eigenmodes and the simulated difference in phase shift imparted to orthogonal eigenmodes.	48
30	Change in the orientation of the electric field vector of eigenmodes as a function of wavelength.	49
31	Change in the reflectivity of the HCG for the orthogonal eigenmodes.	49
32	Change in reflectivity, transmittance, and the normalized absorption loss for a broadband reflector. (Device parameters: $\Lambda a = \Lambda b = 1.508\mu m$, hole radius = $0.569\mu m$, thickness = $560nm$, $n = 2.11$) . . .	52
33	Change in reflectivity, transmittance, and the normalized absorption loss for a high Q reflector. (Device parameters: $\Lambda a = \Lambda b = 1.310\mu m$, hole radius = $0.131\mu m$, thickness = $321.4nm$, $n = 1.943$)	53
34	Comparison of Σ optical losses from experiments with those from simulations.	55
35	Comparison of different components of the optical loss in HCGs for the near horizontal eigenmode.	55
36	Normalized transmission of a focused beam through a new 2D HCG that was fabricated from stoichiometric Si_3N_4	61
37	Toy model of a Fabry-Pérot cavity. Each mirror is modeled as a compound element comprising a lossy medium and a lossless reflector ($T + R = 1$). On each pass through the lossy medium, the amplitude of the electric field is attenuated by factors of $e^{-\gamma_1}$ and $e^{-\gamma_2}$ at mirrors 1 and 2, respectively. The dashed lines indicate the planes at which the reflected, circulating, and transmitted fields are calculated.	63

List of Abbreviations

2Γ	Sum of absorption and scattering losses per round trip in a high finesse cavity
F	Coefficient of finesse
FSR	Free spectral range
HCG	High contrast grating
PhC	Photonic crystal
R	Reflectivity
R_{min}	Minimum of normalized cavity reflection signal
RCWA	Rigorous coupled wave analysis
T	Transmittance
T_{max}	Peak of normalized cavity transmission signal

List of Publications

Portions of this thesis have been drawn from the following publications:

Conference Proceedings

Navin B. Lingaraju; Yichen Shuai; John Lawall; Cavity optomechanics with 2D photonic crystal membrane reflectors. Proc. SPIE 9757, High Contrast Metastructures V, 97570T (March 15, 2016); doi:10.1117/12.2211820.

Chapter 1 Introduction

The field of optomechanics deals with the interaction between light and physical objects through radiation pressure. Optomechanics has received a great deal of attention in recent years because of its potential for application to precision accelerometry [1] chip-scale optical signal processing [2], and fundamental research [3]. There have been comprehensive reviews of the field published recently [4, 5], including one directed to potential applications of optomechanics [6]. Cavity optomechanics is a subset of this field that focuses on the coupling between the optical modes of a cavity and the vibrational modes of a reflective mechanical resonator within the cavity. A popular platform for cavity optomechanics is the so-called “membrane-in-the-middle” arrangement where a reflective membrane serves as the mechanical resonator and is placed within a high finesse optical cavity. In these configurations, it is possible to tune the cavity so as to cool a vibrational mode of the membrane down to the ground state [7].

The focus of this thesis is on a platform slightly different from membrane-in-the-middle systems. Instead of placing a partially reflecting membrane within a high finesse optical cavity, a highly reflective membrane ($R > 99\%$) is used as one of the end mirrors of a high finesse Fabry-Pérot cavity. The mechanical response of the high reflectivity membrane can be modeled as a mass on a spring. When incident light is coupled into the cavity at a wavelength that undergoes a multiple of 2π phase shift per round trip, there is a build up of optical power within the cavity. The circulating optical power in turn exerts a force on the membrane through radiation pressure. As

one can see, the ideal optomechanical element for such a platform has high reflectivity, low mass, and a high mechanical quality factor Q .

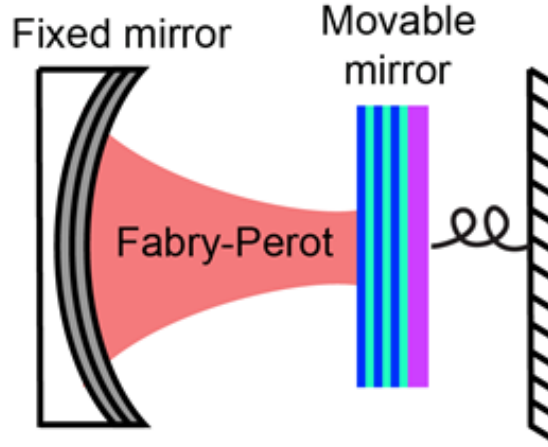


Figure 1: The reflective membrane in Fabry-Pérot cavity can be modeled as a mirror on a spring.

1.1 Cavity Optomechanics and HCGs

In earlier work, freestanding Bragg mirrors [8] and coated cantilevers [9, 10] have been used as the movable mirror in Fabry-Pérot cavities. High contrast gratings offer another way to make low mass, high reflectivity mirrors. In its simplest form, a high contrast grating is a dielectric slab that has been patterned with sub-wavelength scale features to create a periodic modulation of the refractive index in one or two dimensions.

Early work on high contrast gratings (HCGs) focused on devices with periodicity in just one dimension [11, 12]. The 1D index modulation was created by patterning thin (thickness $< \lambda$), high index ($n \geq 2$) films so as to leave behind rectangular segments of the high index material spaced apart at regular intervals. The space

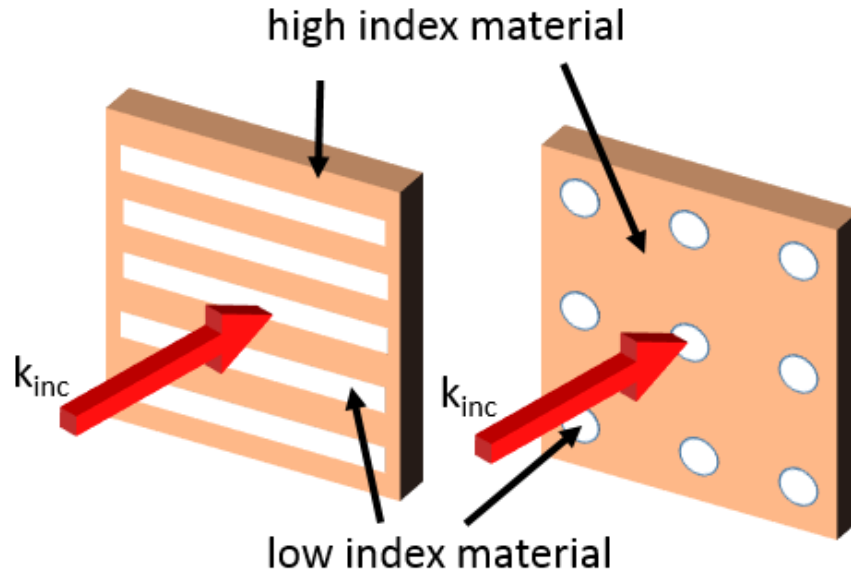


Figure 2: Illustration of a 1D and a 2D high contrast grating.

between these fingers was filled by air, vacuum, or some suitable low index material. By changing the geometry of these devices (width of the fingers or spacing between the fingers), it is possible to engineer them to function as broadband reflectors [13] or as narrowband transmission filters [14].

Owing to their high reflectivity and light weight, high contrast gratings have attracted interest in the field of optomechanics. However, for millimeter sized silicon membranes, the frequency of the fundamental vibrational mode is not high enough to push Fabry-Pérot cavity optomechanical systems into the resolved sideband regime. Stressed silicon nitride on silicon has emerged a leading candidate for such systems. Like silicon, stressed silicon nitride has low optical absorption and is compatible with standard microfabrication processes. Unlike silicon membranes, these films are under great tension and, consequently, have mechanical modes with much higher frequencies.

This advantage comes without any drawback in terms of mechanical losses. Low stress silicon nitride on silicon (SiN_x) is known to exhibit excellent mechanical quality factors ($Q > 10^5$)[15] and the high stress version (stoichiometric Si_3N_4) exhibits Qs an order of magnitude higher [16].

In previous work, our group fabricated 1D HCGs on low stress silicon nitride membranes [17] and, using a Fabry-Pérot cavity [18], optical cooled one of the membrane's vibrational modes down to $T \approx 1\text{K}$.

1.2 Optical Properties of Silicon Nitride and Impact on HCG Performance

This thesis looks to expand on our group's prior work with 1D HCGs in two ways. The first is the fabrication of membrane reflectors based on symmetric, 2D photonic crystal (PhC) patterns, which theory suggests are insensitive to the polarization of light at normal incidence. The benefit of such devices is that they overcome one clear limitation of 1D HCGs - their polarization sensitivity. The other benefit of 2D HCGs has to do with device yield. 2D HCGs are much likelier to survive the fabrication process than their 1D counterparts when PhC patterns get larger than $75\mu\text{m} \times 75\mu\text{m}$. In particular, we found that for 2D HCGs with $300\mu\text{m} \times 300\mu\text{m}$ PhC patterns, the yield was over 90% (only 5 out of 75 devices lost). 1D HCGs with a quarter of these dimensions ($\frac{1}{16}$ the area) had a yield of only 50% [18].

Another type of HCG that would be interesting for cavity optomechanics experiments is a reflector whose spectral response at normal incidence features a sharp reflection peak, i.e., a reflector with a high optical Q. High contrast gratings can be designed to have sharp Fano resonances [19] and such gratings would be particularly

useful in arrangements where the HCG is used as one of the end mirrors in a laser cavity. The asymmetry of Fano resonances would create a similar asymmetry in the round trip gain profile of the laser, thereby making it possible to ensure that the output of the laser is always blue-detuned relative to the peak of the gain profile. Such a laser, in principle, should be capable of cooling the vibrational modes of its own end mirror, i.e., those of the high Q reflector. These HCGs offer another practical advantage. Reflectors with higher optical Qs can ensure single mode operation of the lasers with longer cavity lengths.

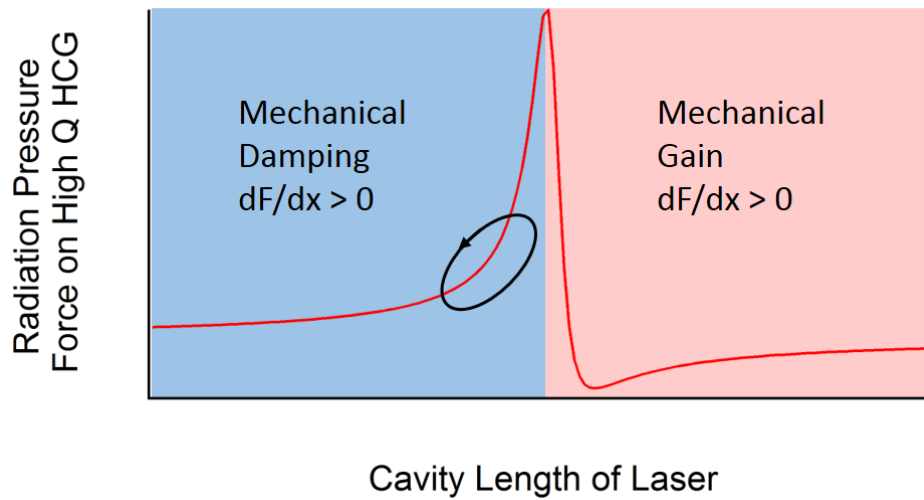


Figure 3: The force exerted by radiation pressure on the end mirrors of a laser cavity depends on the round trip gain profile of the laser. When an HCG with a high optical Q is used as one of the end mirrors, the round trip gain profile is defined, almost entirely, by the spectral response of the HCG. The graph above shows how the force on a high Q reflector changes with the length of the laser cavity. If the cavity length is tuned to ensure that the oscillating mode is blue-detuned, the HCG sweeps out a path similar to the one depicted above.

The performance of the HCGs mentioned above depends critically on the optical properties of the silicon nitride films from which they are fabricated. As will be

shown in later chapters, a slight anisotropy in the refractive index of silicon nitride can make 2D HCGs polarization sensitive, thereby breaking the degeneracy between the polarization eigenmodes of a Fabry-Pérot cavity formed with these devices. With regard to high Q reflectors, it is well established that optical losses, in the form of both scattering and absorption, limit the attainable optical Q [20]. Therefore, there is an important need in the field for techniques to determine the effect of index anisotropy and optical losses on the performance of high contrast gratings.

1.3 Goals and Objectives

The primary goal of this thesis is to study how the optical properties of stressed silicon nitride films impact the performance of 2D HCGs. The work presented in subsequent chapters is focused on three objectives:

- Presenting a new method to precisely determine the reflectivity, transmittance, and losses (scattering + absorption) in high contrast gratings.
- Determining the mechanism responsible for breaking the degeneracy between polarization eigenmodes in Fabry-Pérot cavities where 2D HCGs are used as one of the end mirrors.
- Differentiating between scattering losses and absorption losses in high contrast contrast gratings.

1.4 Outline of Thesis

The current section, chapter 1, offers a brief introduction to the field of cavity optomechanics and provides some context for why high contrast gratings are an attractive element for Fabry-Pérot cavity optomechanical systems. This is followed by a brief discussion of the advantages of stressed silicon nitride films in order to motivate further study of this material system and its optical properties.

Chapter 2 starts by going over a commonly used method to determine mirror reflectivity from measurements of the cavity finesse. Following this, we lay out how information from the cavity reflection signal can be used to arrive at precise estimates for transmission and loss (scattering + absorption) in an HCG. This chapter concludes with some remarks about limitations to using the cavity reflection signal when working with metrastructure reflectors.

Chapter 3 presents data from cavity experiments and connects these results to the optical properties of silicon nitride. The first part of the chapter looks at the polarization sensitivity of 2D high contrast gratings. The discussion is focused on how the separation and orientation of polarization eigenmodes in a Fabry-Pérot cavity with a 2D HCG change with wavelength. The latter half of this chapter is devoted to the results of experiments intended to separate the different components of optical loss (transmission, scattering, absorption) by using the method developed in chapter 2.

In chapter 4, the experimental results are reconciled with predictions from theory and simulations. The chapter begins by introducing a toy model of an HCG in

order to capture the effect of an anisotropic refractive index on cavity measurements. However, this simple model does not account for any of the observed trends as a function of wavelength. This index anisotropy is then incorporated into simulations of HCGs, the results of which exhibit good agreement with experimental data. The chapter concludes with a discussion on using simulations to arrive at an estimate for the absorption loss and then using this estimate to distinguish between the amount of scattering and the amount of absorption in high contrast gratings.

The final chapter, chapter 5, summarizes the results of this thesis and ties it in with the implications they have for experiments in cavity optomechanics. The thesis concludes by suggesting some directions for future work and offers ideas on how to improve device performance.

Chapter 2 Determination of Reflectivity, Transmittance, and Loss

Fabry-Pérot cavities offer a simple way to precisely measure the reflectivity of an uncharacterized reflector. By scanning the wavelength of incident light or by changing the cavity length, one can measure the change in light transmitted by the cavity. The linewidth of this signal and, therefore, the cavity finesse depend on the total optical losses from the cavity. The term loss includes transmission through the mirrors, as well as losses due to absorption and scattering. If the characteristics of one of the mirrors in a Fabry-Pérot cavity are known, then a lumped term corresponding to the sum of all optical losses from the other mirror can be determined with a high degree of precision ($R = 1 - \Sigma$ optical losses).

The clear drawback of this method is that a measurement of the cavity finesse allows one to only measure the reflectivity of a mirror. However, for high contrast gratings, particularly those used in optomechanics systems, it is important to be able to separate the different types of optical losses (transmission, scattering, absorption) from one another. Without such information, one cannot ascertain whether device performance (high reflectivity) is limited by material absorption or whether improvements in fabrication might be able to reduce scattering losses in a meaningful way, for example.

As we will show later in this chapter, cavity measurements generate more data than is normally used when simply determining mirror reflectivity. By recording the normalized peak of the cavity transmission signal and the normalized dip of the cavity reflection signal, one can separate HCG transmission from scattering and absorption

losses.

2.1 Determining Mirror Reflectivity from Cavity Finesse Measurements

A simple optical cavity is shown in figure 2. Light incident from the left is coupled into the cavity, which results in a build up of circulating optical power inside the cavity. A portion of this circulating power is transmitted through the flat mirror and exits the cavity propagating to the right. As the frequency of incident light is varied, sharp peaks are observed in the cavity transmission signal when the phase accumulated per round trip through the cavity is a multiple of 2π .

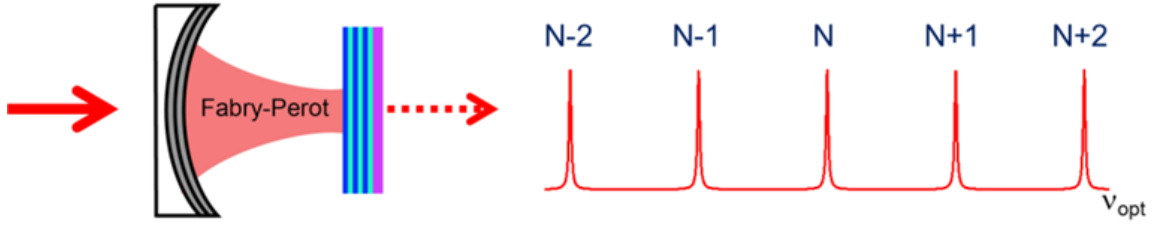


Figure 4: (*left*) Fabry-Pérot cavity showing light incident from the left and exiting the through the flat mirror as the cavity transmission signal. (*right*) Cavity transmission as a function frequency ν_{opt}

The linewidth of the cavity transmission signal, $\Delta\nu_{opt}$, is related to the free spectral range (FSR) and finesse (F) of the cavity.

$$FSR = \frac{c}{2L_{cavity}} \quad (1)$$

$$Finesse = \frac{FSR}{\Delta\nu_{opt}} \quad (2)$$

An estimate of the optical losses from the cavity can be determined from a measurement of the cavity finesse F .

$$F = \frac{2\pi}{\Sigma \text{ optical losses}} \quad (3)$$

Each mirror is defined by a reflectivity (R_1, R_2) , a transmittance (T_1, T_2) , and a lumped term that captures the sum of all scattering and absorption losses $(1 - e^{-2\gamma_1} + 1 - e^{-2\gamma_2})$ in the cavity. The terminology here is borrowed from Siegman [21] and it should be noted that $e^{-\gamma}$ represents the amplitude attenuation after one reflection while $e^{-2\gamma}$ represents the intensity attenuation after one reflection. Therefore, $1 - e^{-2\gamma}$ represents the fractional loss from both scattering and absorption upon reflection. For small losses, which is the case for the high contrast gratings discussed in this thesis, $1 - e^{-2\gamma} \approx 2\gamma$. Therefore, the optical losses from the cavity are given by the sum of $T_1, 2\gamma_1, T_2, 2\gamma_2$. Equation (3) can be recast as:

$$F = \frac{2\pi}{T_1 + 2\gamma_1 + T_2 + 2\gamma_2} \quad (4)$$

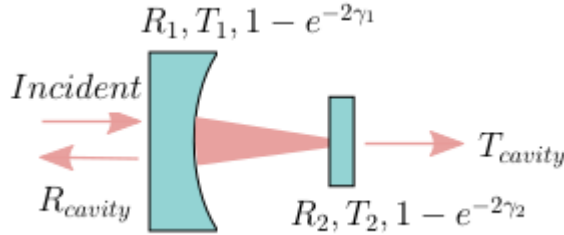


Figure 5: A hemispherical Fabry-Pérot resonator. The net signal propagating from the input face of the first mirror is cavity reflection signal (R_{cavity}). The cavity transmission signal is denoted by T_{cavity} .

However, the sum of all optical losses from each individual mirror is given by $1 - R_{mirror}$, where R_{mirror} is the reflectivity of the particular mirror. Hence, the cavity finesse in terms of the reflectivity of the cavity mirrors is given by:

$$F = \frac{2\pi}{(1 - R_1) + (1 - R_2)} \quad (5)$$

If a Fabry-Pérot cavity is formed from two low loss reflectors, one whose reflectivity is known, then the reflectivity of the other mirror can be determined with a high degrees of precision from the linewidth of the cavity transmission signal. However, knowledge of the cavity finesse is not sufficient to distinguish between outcoupling losses and dissipative losses. As figure 3 makes clear, this arrangement generates more information than simply the linewidth of the cavity resonance. It will soon be shown that additional data from cavity experiments can be used to separate transmission from scattering and absorption losses.

2.2 Cavity Transmission and Cavity Reflection Signals

When the wavelength of light incident on a Fabry-Pérot resonator is scanned across a cavity resonance, a response similar to that shown in figure 6 is observed. R_{cavity} and T_{cavity} represent the total power reflected and transmitted by the Fabry-Pérot resonator as a function of wavelength, respectively.

Consider a cavity similar to the one in figure 5, but where all the characteristics of the input coupler, i.e., the curved mirror, are known ($R_1, T_1, 2\gamma_1$). It can be shown that in order to determine T_2 and $2\gamma_2$ one need only the normalized minimum of the

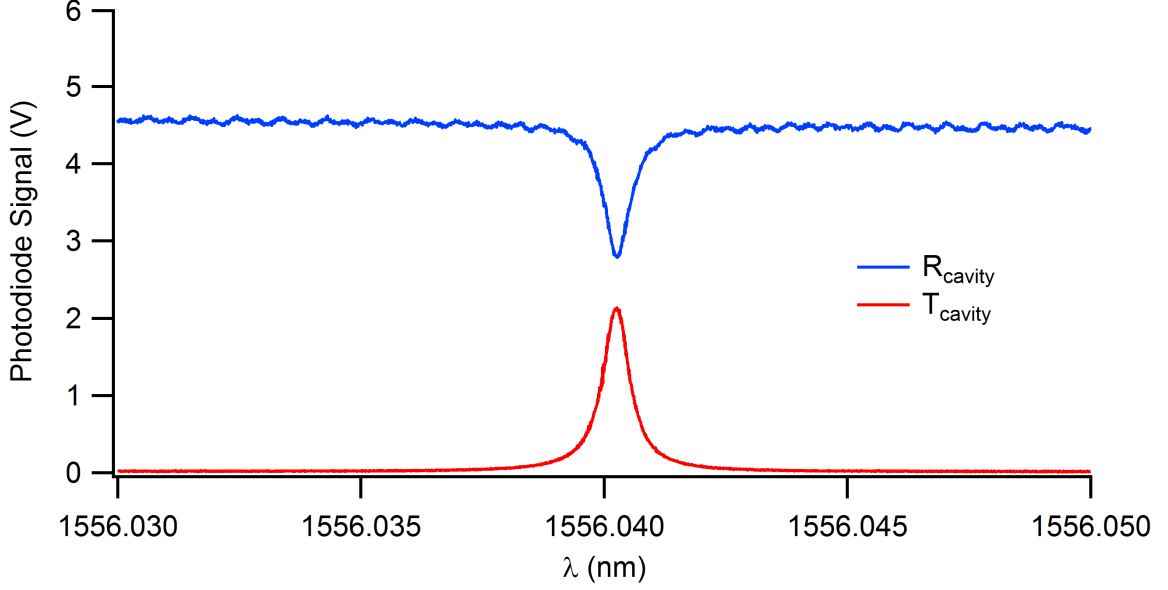


Figure 6: Excerpt of experimental data showing the change in R_{cavity} and T_{cavity} as a function of wavelength.

cavity reflection signal (R_{min}) and the normalized maximum of the cavity transmission signal (T_{max}), both of which occur on resonance. (*See Appendix A for a full derivation relating R_{min} and T_{max} to characteristics of the cavity mirrors.*).

For ease of presentation, 2Γ will be used to denote the sum ($2\gamma_1 + 2\gamma_2$). If $2\gamma_1$ is already known, it is a simple matter to determine $2\gamma_2$ from 2Γ . 2Γ merely represents the total round trip scattering and absorption loss in the cavity. The derivation in Appendix A established that the minimum of the normalized cavity reflection signal (R_{min}) is related to the properties of the cavity mirrors through the relation:

$$R_{min} = \left(\frac{F}{2\pi} \right)^2 (-T_1 + T_2 + 2\Gamma)^2 \quad (6)$$

Equation (4) can be rewritten to give an expression for the round trip absorption and scattering loss:

$$2\Gamma = \left(\frac{2\pi}{F}\right) - T_1 - T_2 \quad (7)$$

Substituting (7) in (6) yields:

$$R_{min} = \left(1 - \frac{T_1 F}{\pi}\right)^2 \quad (8)$$

$$T_1 = \frac{\pi}{F} \left(1 \pm \sqrt{R_{min}}\right) \quad (9)$$

The derivation in Appendix A also established that the properties of the cavity mirrors are related to the normalized peak of the cavity transmission signal (T_{max}) through the expression:

$$T_{max} = \left(\frac{F}{\pi}\right)^2 T_1 T_2 \quad (10)$$

$$T_2 = \left(\frac{\pi}{F}\right)^2 \frac{T_{max}}{T_1} \quad (11)$$

Substituting equation (9) in equation (11) gives:

$$T_2 = \left(\frac{\pi}{F}\right) \frac{T_{max}}{1 \pm \sqrt{R_{min}}} \quad (12)$$

Finally, one can obtain an expression for the round trip absorption and scattering loss by substituting equations (9) and (11) in equation (6):

$$2\Gamma = \left(\frac{\pi}{F}\right) \left(\frac{1 - R_{min} - T_{max}}{1 \pm \sqrt{R_{min}}}\right) \quad (13)$$

Therefore, given R_{min} , T_{max} , and cavity finesse F , one can determine T_1 , T_2 , and 2Γ from equations (9), (12), and (13), respectively.

2.3 Practical Limits and Considerations

There is one obvious complication to using the above expressions to determine the transmittance of the mirrors and the round trip loss due to scattering and absorption in the cavity. The equation for the transmittance of the input coupler, equation (9), yields two solutions. However, this technique is intended to be used in situations where the reflectivity, transmittance, and dissipative losses of one of the mirrors is already known. Depending on which mirror is the uncharacterized mirror, this ambiguity can be resolved by comparing the output of either equation (9) or equation (11) to the transmittance of the mirror whose properties are already known.

The real source of caution when using this approach is to remember that the above analysis assumes perfect mode matching between the input beam and the excited cavity mode, which is usually the fundamental transverse spatial mode. In other words, the analysis assumes that the parameters of the beam (waist size, wavefront curvature, and transverse spatial profile) coupled into the cavity are perfectly matched to those of the excited cavity mode.

In practice, poor mode matching can be remedied (a) by changing the position or power of the converging lens that focuses light onto the input coupler or (b) by

changing the cavity length so that the parameters of the excited cavity mode match those of the incident beam. Poor mode matching can also occur because of distortions in the spatial profile of light that is coupled into the cavity. Such distortions can be minimized by reducing the number of optical elements upstream of the cavity or by ensuring that the input coupler does not introduce significant artifacts to light coupled into the cavity.

Imperfect mode matching manifests through excitation of higher order transverse modes of the cavity. When the wavelength of incident light, or the cavity length, is swept to cover one free spectral range, higher order modes will register as peaks on the cavity transmission signal albeit at frequencies slightly offset from the fundamental transverse mode. However, it is possible to use data that registers the excitation of higher order modes to compensate for their effect on the measured values of R_{min} and T_{max} of the fundamental mode.

2.4 Cavity Configurations

The technique presented in the previous sections was described in very general terms. The principal interest of this thesis is to measure R , T , and 2γ for high contrast gratings. In order to do so, one would simply construct a cavity similar to the one in figure 5, but where a high contrast grating is used in place of the flat mirror and where the curved mirror is one whose properties ($R_{dielectric}$, $T_{dielectric}$, $2\gamma_{dielectric}$) are already known. As has been established, this information in conjunction with the normalized minimum of the cavity reflection signal (R_{min}) and the normalized maximum of the cavity transmission signal (T_{max}) is sufficient to determine the reflectivity, transmit-

tance, and dissipative losses of the other mirror, i.e., the high contrast grating.

The hemispherical cavity described above, where an HCG takes the place of the flat mirror, can be used in one of two configurations - one where the dielectric mirror is used as the input coupler (*below left*) and one where the HCG is used as the input coupler (*below right*).

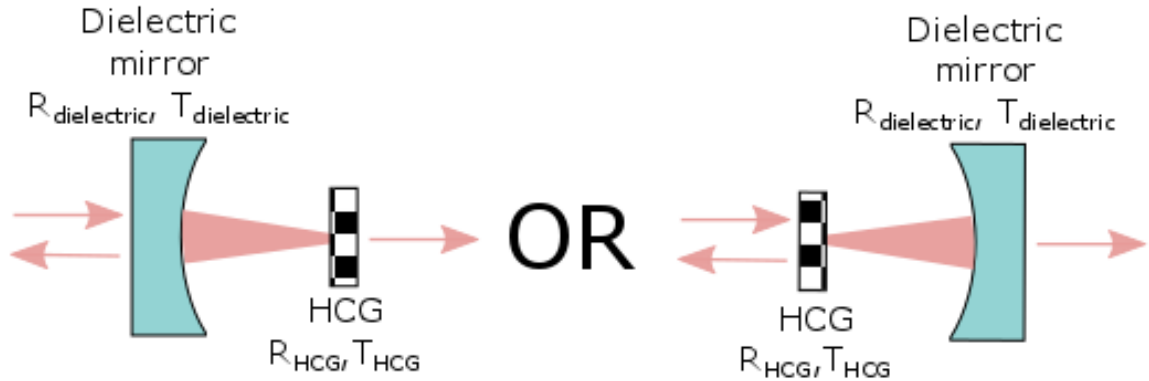


Figure 7: Alternate configurations for cavity measurements

2.4.1 HCG Input Coupler

From the perspective of assembling cavities for experiments, this configuration is easier to work with. Since the HCG is very thin, as compared to a dielectric mirror, it is a trivial matter to focus the incident beam down to its waist just inside the cavity. This makes it possible to achieve good mode matching between the incident beam and the fundamental transverse mode of the cavity.

However, this configuration has one significant drawback, a drawback that is particular to high contrast gratings. To ensure good mode matching to the fundamental transverse mode of the cavity, light transmitted into the cavity by the input coupler

needs to have a clean Gaussian profile. However, it was found that the HCGs we used introduced a fair amount of distortion to transmitted light, especially at wavelengths near the mirror's peak reflectivity. In other words, at these wavelengths, the transverse spatial profile of light entering the cavity is not Gaussian and, consequently, this leads to the excitation of higher order modes in the cavity. Since there is less light coupled into the cavity that is mode matched to the fundamental, the transmission maximum at resonance will be lower than the expected. Since there is also a smaller than expected buildup of circulating power in the fundamental transverse mode, the reflection dip measured at resonance will be higher than for the case of ideal mode matching.

The distortion introduced into transmitted light by the HCG affects the cavity reflection signal in another way. The cavity reflection signal is actually the superposition of two waves - incident light that is promptly reflected off the input coupler and light circulating in the cavity that is transmitted through the input coupler. Distortion in the latter affects the measured value of R_{min} , thereby reducing the accuracy of measurement in this configuration.

2.4.2 HCG Output Coupler

The only real drawback to this configuration, from a practical standpoint, is that it can be tedious to position the curved dielectric mirror such that light transmitted by it is mode matched with the fundamental transverse mode of the cavity. However, there are some advantages to using this cavity arrangement. Since high quality dielectric mirrors with low loss and low distortion are readily available, the incident beam is

less likely to pick up significant distortion on its way through the dielectric mirror (input coupler) and into the cavity. Although the HCG distorts transmitted light, this has no effect on cavity transmission signal, which is simply a measurement of the total intensity transmitted by the cavity in the forward direction.

The second benefit of this arrangement is that it allows one to quickly determine the proper sign in front of $\sqrt{R_{min}}$ in equation (9) because the transmittance of the dielectric mirror is already known. With this information in hand, values for the HCG transmittance (T_2), as well as the the round trip scattering and absorption loss (2Γ), can be determined from equations (11) and (13).

2.5 Summary

This chapter presented an overview of a commonly used method to estimate R for a high reflectivity mirror ($R \approx 1$). This technique only needs to be supplemented by measurements of T_{max} and R_{min} in order to distinguish between transmittance from scattering and absorption losses in a high reflectivity mirror.

While there are some practical advantages to using a cavity where the HCG is the input coupler, these advantages are likely erased because the HCG introduces a good amount of distortion to transmitted light in the wavelength range where its reflectivity is the highest. Although the second arrangement, where the HCG is used as the cavity's output coupler, can be a challenge to assemble and tune, it imposes no artificial limit on the quality of mode matching that can be attained.

Chapter 3 Measurement of HCG Performance

As mentioned in the first chapter, there is an interest in 2D HCGs because they are better able to withstand the fabrication process, thereby making it possible to fabricate devices with much larger areas. From the standpoint of cavity optomechanics, there is an interest in fabricating polarization-insensitive broadband reflectors, as well as narrowband (high Q) filters. Attaining high cavity finesse is particularly important for optomechanics experiments and so most of our focus is on designs where the HCG reflectivity approaches unity. Making use of cavity reflection signal in the manner suggested by the previous chapter makes it possible to measure the reflectivity, transmittance, and loss down to a hundredth of a percent.

The first part of this chapter focuses on the unexpected polarization sensitivity of 2D HCGs based on symmetric photonic crystal patterns. In particular, Fabry-Pérot resonators formed using these HCGs supported two nondegenerate polarization eigenmodes and the orientation of these eigenmodes changed with wavelength. The latter half of this chapter presents results from the new measurement technique. Estimates for the transmittance of the dielectric mirror are shown to have good agreement with the known values for this mirror. This information is then used to determine T_{HCG} and 2Γ .

3.1 HCG Fabrication

2D high contrast gratings were fabricated by first growing a 600nm thick film of low-stress silicon nitride on silicon (100). A 4 x 4 array of windows were then

etched from backside of the wafer up to the silicon nitride film to leave behind 16 suspended membranes. Using e-beam lithography, 2D photonic crystal patterns (square - $300\mu m \times 300\mu m$ or circular - $d = 300\mu m$) were written onto photoresist, which was later developed to leave behind a mask. Finally, reactive ion etching was used to transfer the 2D photonic crystal patterns to the center of their respective membranes. All 16 membranes on a chip had a 2D photonic crystal pattern. The patterns had slightly different lattice parameters from one another and the parameters were chosen specifically to obtain broadband reflectivity in the telecom band.

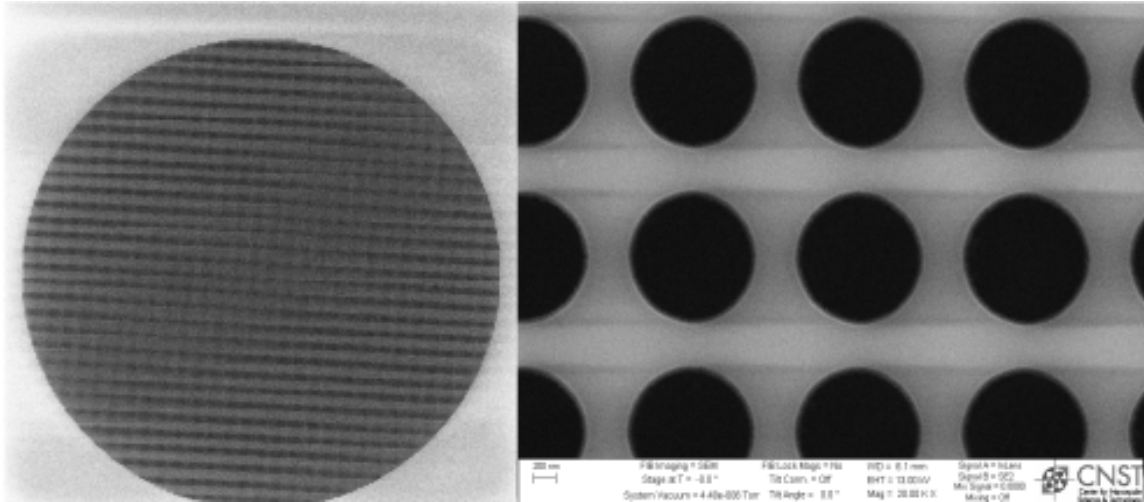


Figure 8: (*left*) SEM images showing the photonic crystal pattern inscribed within a circular region of the membrane. (*right*) Close up of a few unit cells of the lattice.

3.2 Cavity Experiments

Initial experiments focused on determining the reflectivity from on measurements of the cavity finesse. The new 2D HCGs were used as the flat mirror of a hemispherical Fabry-Pérot resonator and a broadband dielectric mirror ($R_{curvature} = 50mm$) was used for the curved mirror. The dielectric mirror was chosen such that it had a

reflectivity significantly higher ($1 - R = 1.6 * 10^{-4}$) than what was expected for any of the individual HCGs over the wavelength range of interest (1520nm – 1600nm). As a result, the linewidth of a cavity resonance, or any other measure of cavity performance, was limited by the optical losses of the HCG.

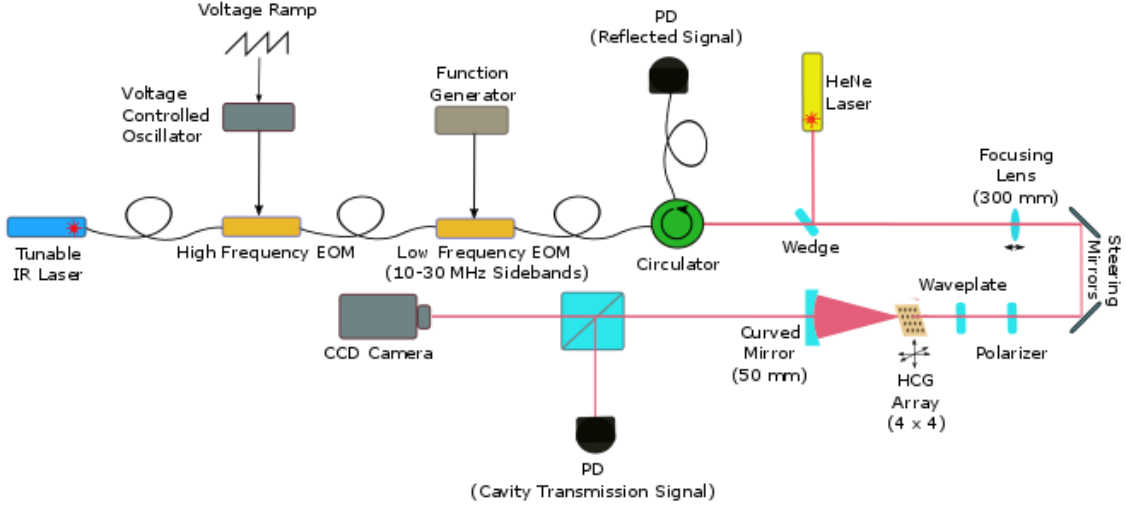


Figure 9: Setup of cavity experiment used to determine the reflectivity of HCGs.

A laser, tunable over the telecom band, was used to excite the modes of the cavity. Since these measurements were made with a long cavity ($L_{cavity} \approx R_{curvature}$), light coupled into the cavity only needed to be swept over a small frequency range (tens of MHz) in order to measure the linewidth of a cavity resonance. An electro-optic phase modulator was used to put sidebands on the output of the laser and the cavity was tuned to couple to one of the sidebands. By driving the electro-optic phase modulator with the output of a voltage-controlled oscillator (VCO), the sidebands were made to sweep out a range in frequency space. Since the VCO was driven by a voltage ramp, the frequency of the sidebands varied linearly with time. A 2 volt ramp was supplied to the VCO, which corresponded to a frequency sweep of about 150 MHz or

a wavelength scan covering 12pm in the C-band.

A second electro-optic phase modulator was used to put a set of low, fixed-frequency sidebands (tens of MHz) on the output of the first EO phase modulator. This was done in order to establish a frequency reference on the cavity transmission signal. The cavity transmission signal is recorded on an oscilloscope and is recorded as a function of time. The frequency of the sideband that couples to the cavity is swept in a linear manner over that time frame. By determining the separation between the two, fixed-frequency sidebands produced by the second EO phase modulator, one can convert the cavity transmission signal from a function of time to a function of frequency. Depending on the strength and linewidth of the transmitted signal, carrier-sideband separations of 10 MHz, 20 MHz, or 30 MHz were used as frequency references.

The output of the second phase modulator is sent through a circulator in order collect to light reflected back from the cavity. Downstream of the circulator, a wedge is used to combine infrared light from the tunable laser with red light from a HeNe laser in order to produce a visible beam that co-propagates with the IR beam. Aside from being useful for optical alignment, the co-propagating red light helps park the laser on a membrane's photonic crystal pattern, which is a tiny $300\mu m \times 300\mu m$ target. When light from the HeNe laser is incident on the photonic crystal pattern, a characteristic diffraction pattern is observed in the far field. A polarizer followed by a half waveplate is placed after the wedge in order to control the polarization of light incident on the cavity. Light transmitted by the cavity passes through a non-polarizing beam splitter (NPBS). One beam is sent to a photodetector and picked up

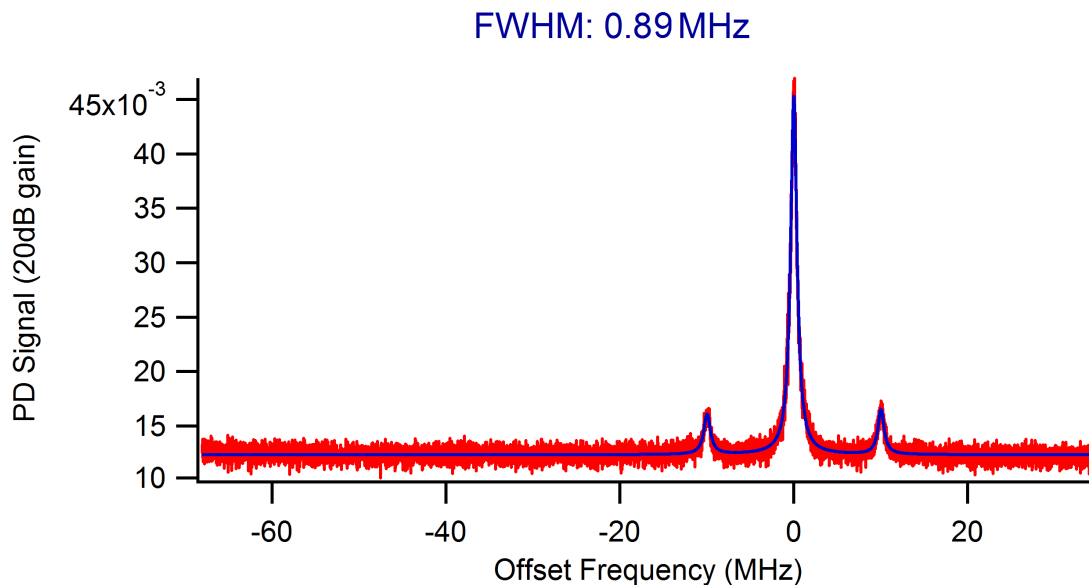


Figure 10: The second EO phase modulator generates two sidebands, which are offset by 10MHz from the carrier. The sideband-sideband spacing of 20Mz is used to convert the bottom axis of the oscilloscope trade from one of time to one of frequency. Based on this frequency reference, the linewidth of the carrier above estimated to be 890kHz full width at half maximum (FWHM).

on an oscilloscope. As shown in figure 10, the photodetector signal can be used to calculate the linewidth of a cavity resonance. The other beam exiting the NPBS is imaged on a CCD camera in order to visualize the excited transverse spatial modes of the cavity.

3.3 HCG Reflectivity

Light incident on a Fabry-Pérot cavity, which is a mode-selective resonator, does not couple to all possible transverse modes of cavity. The coefficients of finesse are different for, and particular to, each excited mode. Therefore, if one is interested in the reflectivity of an HCG under a Gaussian beam, the experiment must be tuned to efficiently excite only the fundamental transverse mode of the cavity.

The output of the first electro-optic phase modulator comprises a carrier and two sidebands. The offset of the sidebands from the carrier varies linearly with time, thus mimicking a frequency-swept light source. Therefore, a readout of the cavity transmission signal contains information about the frequency response of the cavity. When the frequency of one of the sidebands scans across a cavity resonance, a characteristic Lorentzian lineshape will register on the cavity transmission signal.

The linewidth of cavity resonances was recorded at various wavelengths over the wavelength range from 1540nm – 1580nm. The reflectivity of the HCG outside these wavelengths was too low to generate a strong cavity transmission signal. For this HCG, the narrowest cavity resonance linewidths occurred between 1550nm and 1560nm and ranged from 3MHz to as low as 0.80MHz. The FSR of the cavity was measured to be 3.13GHz, which corresponded to a cavity length of 49.5mm. The coefficient of finesse of the cavity was determined from equation (2) and the results are illustrated in figure 11.

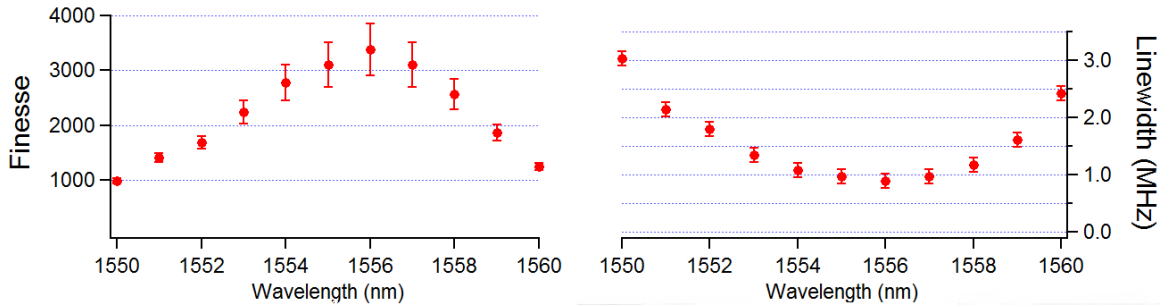


Figure 11: (*left*) Calculated coefficients of finesse over wavelengths from 1550nm-1560nm. (*right*) Corresponding cavity resonance linewidths.

Since the reflectivity of the dielectric mirror is known, equation (5) can be used to determine the reflectivity of the HCG from the estimated cavity finesse at various

wavelengths. The reflectivity calculated in this manner was compared to the results of a simple transmission test where incident light was focused onto the HCG and the fraction of light transmitted was measured. As figure 12 makes clear, straightforward measurement of light transmitted by the HCG is not a good barometer of HCG performance.

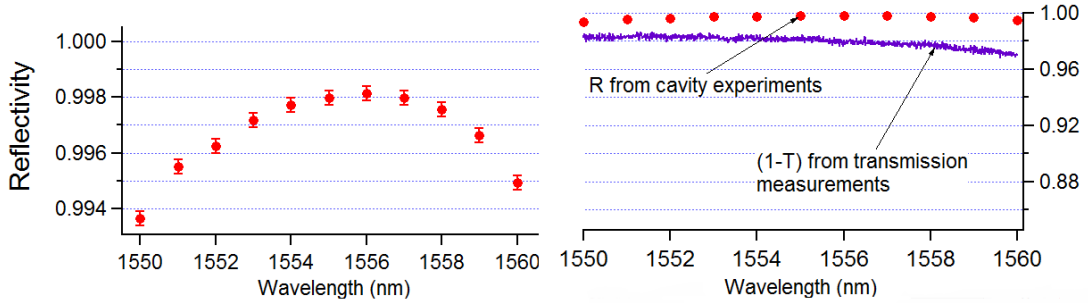


Figure 12: (*left*) Calculated HCG reflectivity over the wavelengths from 1550nm-1560nm. (*right*) Comparison between cavity experiments (R_{HCG}) and simple transmission measurements ($1 - T_{HCG}$).

3.4 Nondegenerate Polarization Eigenmodes

When the cavity is tuned to excite only the fundamental transverse mode, resonances should be separated from each other by the free spectral range of the cavity. However, as the results in figure 13 show, cavity resonances were observed in pairs of closely spaced peaks. The separation between the resonances in each pair was small (tens of MHz) compared to the FSR of the cavity (3.13GHz). The occurrence of two closely spaced resonances could be explained by either excitation of higher order transverse modes of the cavity or birefringence in one of the mirrors.

A CCD camera was used to monitor the transverse spatial profile of light exiting

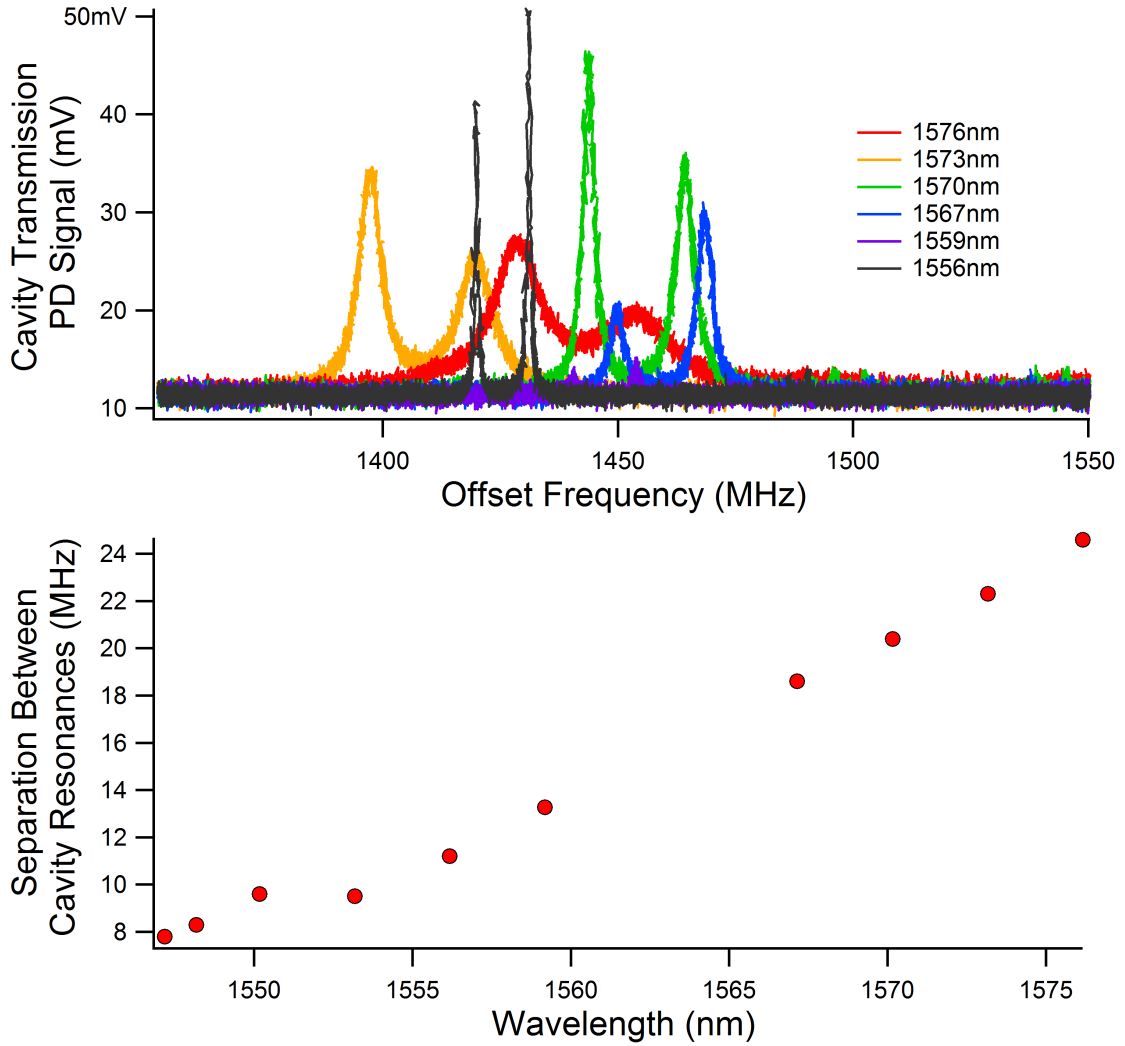


Figure 13: (*top*) Cavity transmission signals measured at various wavelengths. (*bottom*) Frequency offset between closely spaced cavity resonances as a function of wavelength.

the cavity. The excitation of any higher order transverse modes would be visible on the video output of the CCD. Video did not reveal much coupling, if any, to higher order modes when the wavelength of incident light source was swept across a free spectral range. In order to be certain that this was the case, Pound-Drever-Hall laser frequency stabilization [22] was used to lock the frequency of the sidebands output from the first electro-optic modulator to each cavity resonance. The cavity

transmission signal had a Gaussian profile regardless of which resonance in a pair of closely spaced peaks the laser was locked to. In other words, the cavity supported two fundamental transverse modes that were offset from each other by only tens of megahertz. This separation was significantly smaller than the free spectral range of the cavity, which was approximately 3GHz. This suggested that one of the cavity mirrors was birefringent.

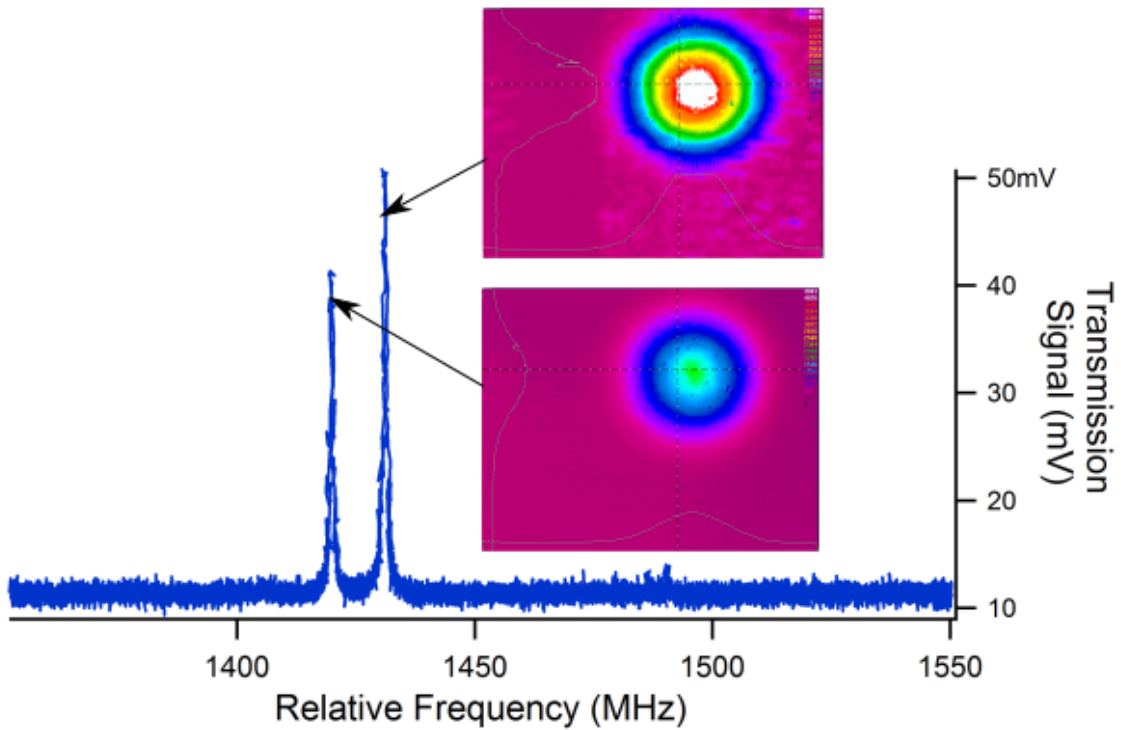


Figure 14: Oscilloscope trace of the cavity transmission signal when circularly polarized light is incident on the cavity. The insets show the transverse profile of the transmitted beam when the laser was locked to the corresponding peak.

In earlier experiments, the dielectric mirror was paired with a flat mirror of known reflectivity and characterized using a cavity. Those experiments did not reveal closely spaced resonances like those seen in figure 13. This leaves the HCG as the only poten-

tial source of birefringence even though the 2D HCGs fabricated were, theoretically, expected to be polarization insensitive. To identify the orientation of two possible polarization eigenmodes, the laser was locked to each resonance and a polarizer placed between the cavity and a downstream power meter. By rotating the polarizer and recording the output of the power meter, the fraction of power in the transmitted beam at different angles was charted (see figure 15). The eigenmodes were found to be linearly polarized and were inclined at 20.5 degrees with respect to the horizontal and vertical axes.

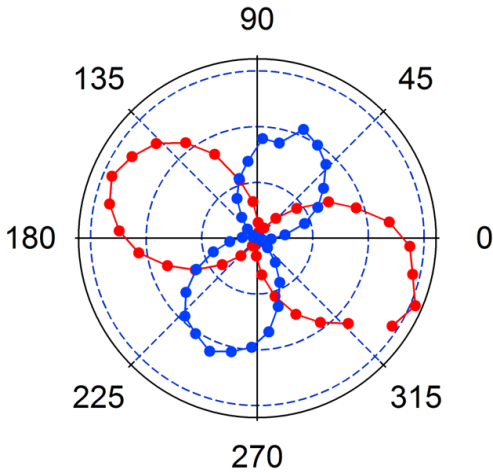


Figure 15: The cavity was locked to each of two closely spaced cavity resonances. The power in the transmitted signal was analyzed in increments of 10 degrees using a polarizer and the results recorded on a polar plot.

The eigenmodes also had different linewidths. By changing the polarization of incident light to match the orientation of one of the eigenmodes, it was possible to excite only that particular eigenmode during a sweep of the wavelength. The eigenmode inclined at 20.5 degrees from the vertical axis had a narrower resonance linewidth. The respective linewidths at 1556nm were found to be $0.66 \pm 0.006 MHz$

and $0.83 \pm 0.015MHz$, respectively.

3.5 Short Cavity with HCG Output Coupler

To make measurements using the new technique presented in chapter 2, the experiment setup in figure 9 was modified in two ways. First, the cavity was reconfigured to use the HCG as the output coupler of the systems. Additionally, instead of using a cavity length close to the stability boundary ($L_{cavity} \approx 50mm$), the cavity length was reduced to below a millimeter. Care was taken to ensure that the spot size of the fundamental transverse mode on the HCG for the short cavity was the same as it was for the long cavity.

The reduction in cavity length practical advantages. The separation between the mirrors was reduced to around 0.4mm, which corresponded to a free spectral range in excess of 300GHz. In other words, in the telecom band, resonances for a given eigenmode were spaced apart by approximately 3nm in wavelength space. For such high FSRs, electro-optic phase modulators were no longer needed to create a frequency-swept light source. The tunable laser, which was capable of executing wavelength sweeps over the range from 1500nm-1620nm, was instead directly used as the frequency-swept source.

3.5.1 HCG Reflectivity

As was done for the long cavity, the linewidths of cavity resonances at various wavelengths were measured. This was done for both polarization eigenmodes and the corresponding coefficients of finesse and HCG reflectivities are shown in figure 17.

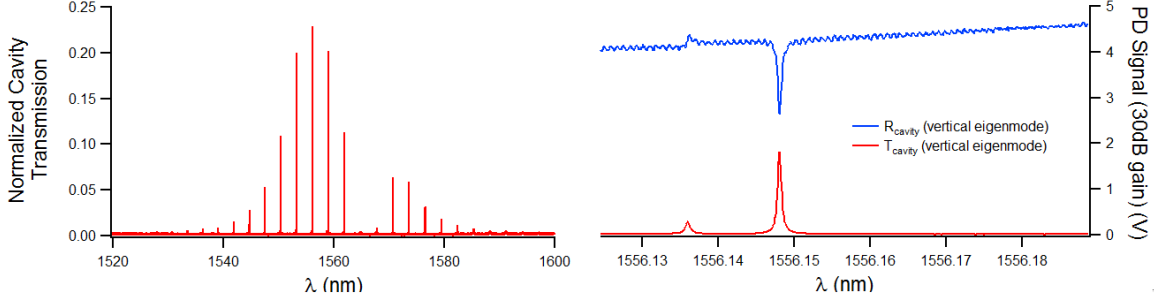


Figure 16: (*left*) Normalized cavity transmission signal over the wavelength range from 1520nm - 1600nm. (*right*) Raw cavity transmission and reflection signals around 1556nm, the region of highest reflectivity.

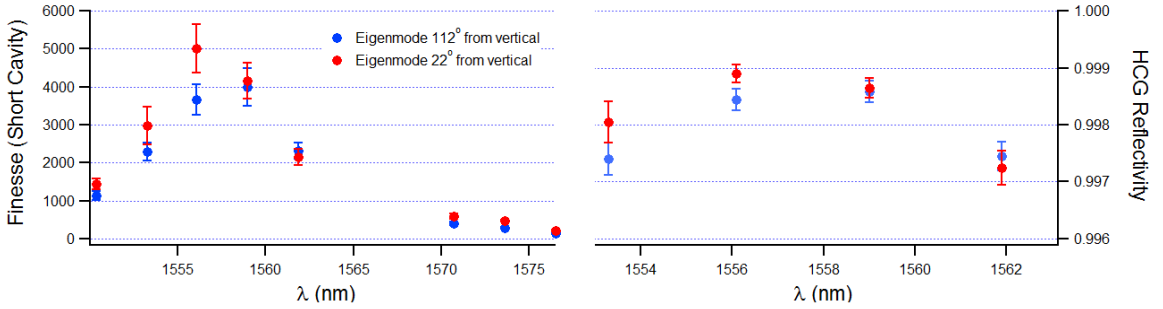


Figure 17: (*left*) Cavity finesse as a function of wavelength for both polarization eigenmodes. (*right*) Inferred HCG reflectivity over the range from 1553nm - 1563nm.

One difference that stands out between the results for the short cavity compared to those for the long cavity (see figure 11) is that higher coefficients of finesse were obtained with the short cavity. Since the same set of mirrors were used in both experiments, one should expect both cavities to have the same finesse since the finesse is merely a function of the total optical losses from the cavity.

There are some factors that would explain such a discrepancy. One is that despite our best efforts, the spot size of the excited mode at the HCG was different in both experiments, which resulted in electric field profiles that "saw" different numbers of photonic crystal unit cells. The other is that excited modes for the two cavities

were excited on different portions of the same photonic crystal pattern, one portion presumably having fewer imperfections than the other. Although the divergence in results is perplexing and worthy of additional study, the purpose of our work was to determine an upper limit for HCG performance in a practical setting. The results from the short cavity establish that the 2D HCGs are capable of attaining reflectivities $\cong 99.9\%$.

3.5.2 Properties of Polarization Eigenmodes

Since the same elements were used in the short cavity as were used in the long cavity, the short cavity too supported closely spaced polarization eigenmodes. The wavelength separation between the each pair of eigenmodes was measured. In order to compare these results with those from the long cavity, the respective eigenmode separations are rewritten in terms of the difference in phase shift imparted by the HCG to each of the eigenmodes ($\Delta\phi$).

The two polarization eigenmodes are very close to each other in frequency space and, therefore, satisfy the same multiple of 2π phase shift per round trip. Therefore, if one eigenmode has a resonance at λ_1 and the other eigenmode has a nearby resonance at λ_2 ,

$$2\pi \left[\frac{2 * L_{cavity}}{\lambda_1} \right] + \phi_1 = 2\pi \left[\frac{2 * L_{cavity}}{\lambda_2} \right] + \phi_2 \quad (14)$$

Rearranging the terms gives an expression for the difference in phase shift ($\Delta\phi$) imparted by the HCG to the two eigenmodes:

$$\Delta\phi = 4\pi * L_{cavity} \left[\frac{1}{\lambda_1} - \frac{1}{\lambda_2} \right] \quad (15)$$

$\Delta\phi$ can be expressed in terms of the wavelength separation between orthogonal eigenmodes (as measured in the case of the short cavity),

$$\Delta\phi \approx \frac{4\pi * L_{cavity}}{\lambda^2} [\lambda_2 - \lambda_1] \quad (16)$$

or in terms of the frequency separation between orthogonal eigenmodes (as measured in the case of the long cavity).

$$\Delta\phi = \frac{4\pi * L_{cavity}}{c} [f_1 - f_2] \quad (17)$$

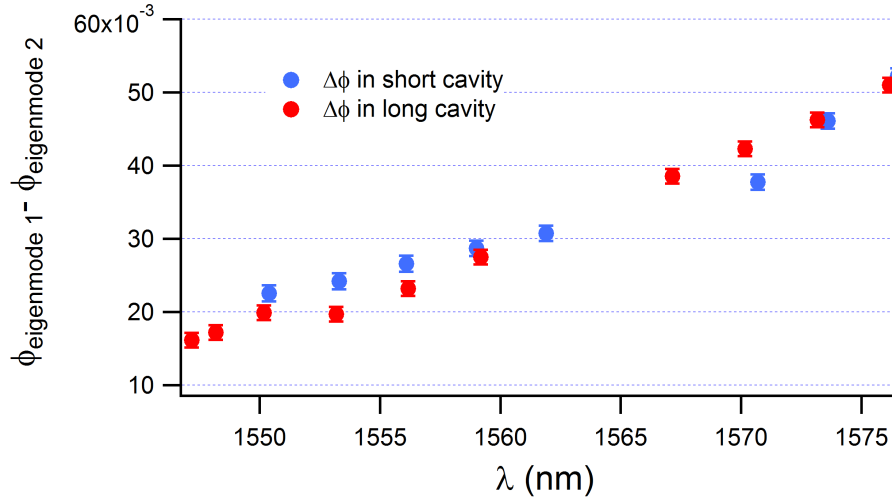


Figure 18: Difference in phase shift imparted by the HCG to the eigenmodes based on data from both the long ($L_{cavity} = 49.5mm$) and short cavity ($L_{cavity} = 0.42mm$)

Using the above relationships, data for eigenmode separation as a function of wavelength for both the long cavity (in terms of MHz) and the short cavity (in terms

of nm) can be converted into an inferred difference in phase shift imparted by the HCG to each of the polarization eigenmodes.

While there is agreement between the two data sets, this does not help determine the source of birefringence in the HCG. In addition to the wavelength-dependent difference in phase shift imparted by the HCG upon reflection, it was also observed that the orientation of the eigenmodes varies with wavelength. Figure 19 catalogs how the orientation of the linearly polarized eigenmodes changes with wavelength.

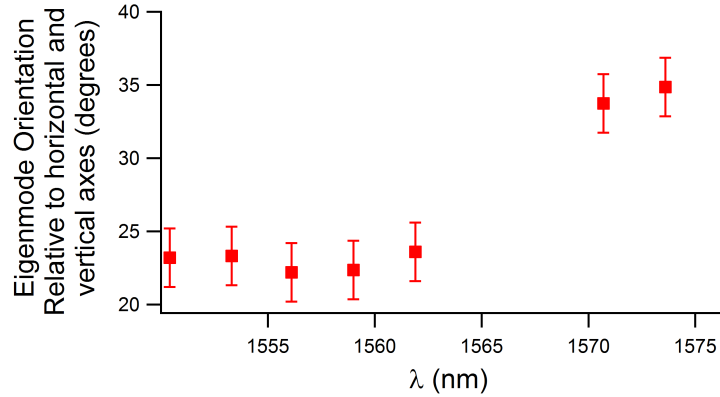


Figure 19: Orientation of the linearly polarized eigenmodes relative to the horizontal and vertical axes.

3.5.3 “Anomalous Peak”

In figures 16, 17, 18, and 19 there is a conspicuous lack of data for the wavelength range between 1562nm and 1570nm . This lack of data can be explained by figure 20. This shows the results for an experiment where a Gaussian beam was focused onto the HCG and transmission through the grating was recorded on a power meter. What stands out in this graph is the presence of a narrow transmission peak within a region of high reflectivity.

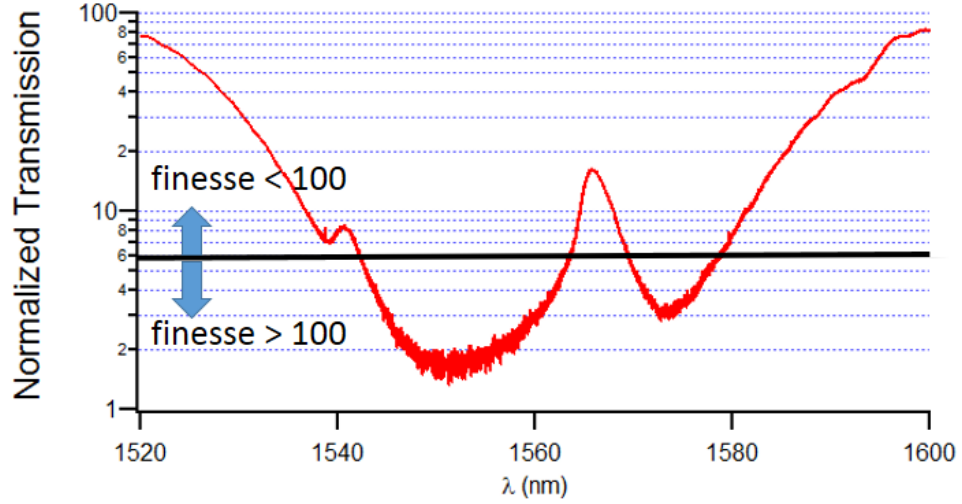


Figure 20: Normalized transmission of a focused beam through the 2D HCG. When this HCG is used as the end mirror in a Fabry-Pérot cavity, the coefficient of finesse drops below 100 for values of transmission over 6%.

All of the data in figures 16, 17, 18, and 19 were derived from cavity measurements. When the finesse drops below 100, the linewidths of the cavity resonances become very broad ($> 50\text{MHz}$ in the long cavity) and peaks of the cavity transmission signal become very small. The net effect is that the characteristic Lorentzian lineshape gets “washed out.” As the crude measurement in figure 20 makes clear, it is very difficult to pick up any cavity resonances over the wavelength range from 1563nm to about 1568nm . Consequently, there is no data from cavity measurements over this range.

3.6 Separation of HCG Transmittance from Scattering and Absorption Loss

In order to determine the transmittance and loss due to the HCG, the minima in the normalized cavity reflection signal (R_{min}) and the maxima in the normalized cavity transmission signal (T_{max}) were tabulated. R_{min} and T_{max} for the near vertical polarization eigenmode are shown in figure 21 below. These data, coupled

with information about the cavity finesse, was used to arrive at an estimate for the transmittance of the cavity's input coupler, i.e., the curved dielectric mirror. Since this mirror's optical losses were already known ($1 - R_{dielectric} = 1.6 * 10^{-4}$), both solutions to equation (9) were evaluated against this predetermined value. As illustrated by the graph on right in figure 21, the second solution to equation (9) ($T_{dielectric} = \frac{\pi}{F}(1 - \sqrt{R_{min}})$) shows much better agreement with the known value for the optical losses of the dielectric mirror.

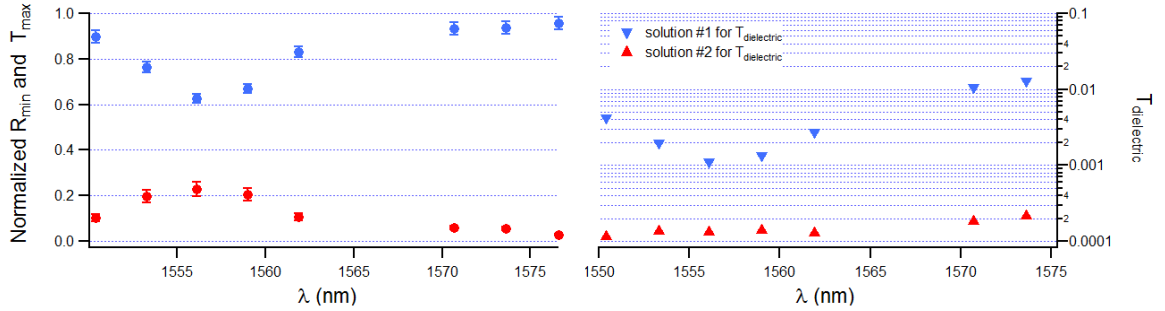


Figure 21: (left) R_{min} and T_{max} for the near vertical polarization eigenmode. (right) Possible solutions for $T_{dielectric}$. (NOTE: Optical losses (transmission + absorption + scattering) from the dielectric mirror are known to be $\cong 0.00015$.)

With the proper solution for $T_{dielectric}$ in hand, the transmittance of the HCG was determined from equation (11) and the sum of all round trip scattering and absorption losses 2Γ calculated from equation (13). In the region of highest HCG reflectivity, optical loss due to transmission is on the same order as loss due to scattering and absorption. As the next chapter will show, further reductions to absorption loss primarily boost HCG reflectivity without much, if any, effect on HCG transmittance. In other words, it is unlikely that R_{HCG} can be pushed past 99.95%.

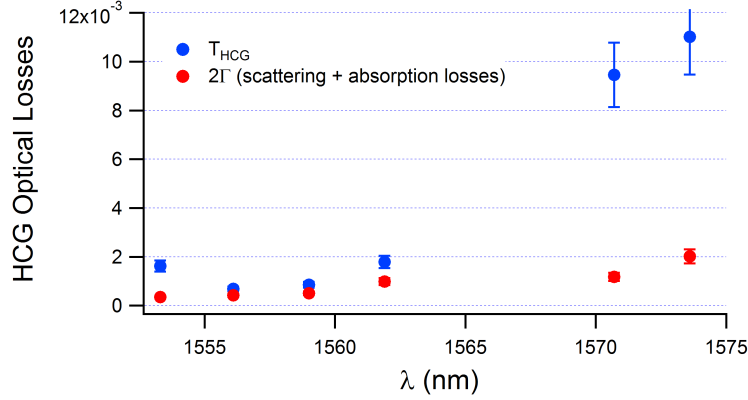


Figure 22: Optical losses from the HCG are separated into HCG transmittance and a lumped quantity that captures the total scattering and absorption loss.

3.7 Summary

It is clear that low stress silicon nitride membranes patterned with a 2D photonic crystal lattice indeed function as high-reflectivity, broadband mirrors. However, these devices were not insensitive to polarization as predicted. The reflectors exhibit a very small amount of birefringence, which is only detectable because of the high reflectivity of the HCGs. In a device with a slightly lower reflectivity, the linewidths of the two polarization eigenmodes would be large enough that they would overlap with one another and register as only a single peak in the cavity transmission signal.

There are two possible sources for the HCG's birefringence. The most obvious one is that the fabrication process introduces some asymmetry into the 2D photonic crystal pattern. The other possibility is that the refractive index of silicon nitride is not isotropic. A small anisotropy in the membrane's refractive index could introduce birefringence much in the same way it does for a bare dielectric material. Arguing in favor of the second possibility is the fact that the orientation of the polarization

eigenmodes changes with wavelength. As we will show in the subsequent chapter, the source of birefringence in these 2D HCGs is decidedly the result of anisotropy in the refractive index of stressed silicon nitride.

Finally, by using the HCG as the output coupler in a short cavity, it was shown that the components of optical loss in a cavity could be separated from one another. Estimates for the transmittance of the dielectric mirror, the transmittance of the HCG, and the round trip losses from the cavity were determined by a simple extension of cavity experiments commonly used to measure mirror reflectivity. Furthermore, these results illustrate that HCG performance is not solely limited by scattering and absorption losses. Although these losses cannot be separated by the current technique, there is potential for simulations to aid in separating scattering losses from absorption losses, as will be shown in the next chapter.

4.1 Anisotropic Refractive Index in Stressed Silicon Nitride

The curved dielectric mirror used in cavity experiments presented in the last chapter was initially characterized in the same manner as the HCG. In other words, a Fabry-Pérot cavity consisting of the curved dielectric mirror and a flat reference mirror (of as high or higher reflectivity) was used to determine the sum of all optical losses ($1 - R$) from the curved dielectric mirror. No nondegenerate polarization eigenmodes were observed at any point during this process. Therefore, one is left to conclude that it is something in the HCGs that breaks the degeneracy between the polarization eigenmodes in a Fabry-Pérot cavity where a 2D HCG is used as an end mirror.

One possible source for this phenomenon is a slight anisotropy in the refractive index of the stressed silicon nitride film on which our 2D HCGs were fabricated. To potentially arrive at an analytic solution that captures the behavior described above, we develop a toy model that introduces a mechanism to impart the phase shifts referenced in equation (14). The simplest construction that accomplishes this is a compound element consisting of a perfectly transmitting wave retarder and a high reflectivity mirror.

4.1.1 Toy Model HCG

A Fabry-Pérot cavity comprising the toy model HCG is shown in figure 23. The wave retarder portion of the toy model has a fast axis aligned with the x-axis of the system and the mirror portion of the toy model is characterized by complex reflection

and transmission coefficients ρ_2 and τ_2 , respectively. The difference in phase shift imparted by the wave retarder per pass is denoted by ϕ . Linearly polarized light is incident on the first mirror (ρ_1, τ_1), a portion of which couples into the cavity and leads to a build up of circulating intensity (I_{circ}). A fraction of the circulating intensity exits the cavity (I_{trans}) and corresponds to the cavity transmission signal. The electric field of the incident field is oriented at an angle θ with respect to the x-axis.

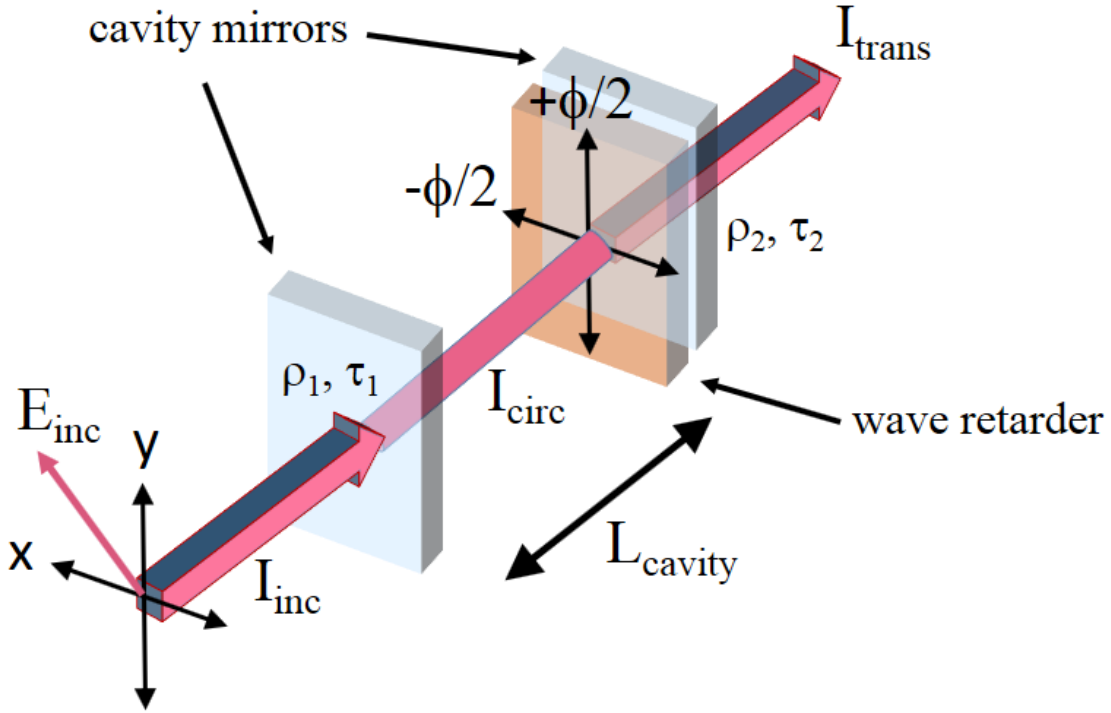


Figure 23: Cavity where the HCG is modeled as a compound element consisting of a perfectly transmitting wave retarder and a high reflectivity mirror.

This cavity features polarization eigenmodes oriented along the x- and y-axes of the system. Therefore, the effect of the x- and y- components of the incident field can be treated separately. In the steady state, the x-component of the circulating field

just in front of the first mirror inside the cavity is given by:

$$E_{circ,x} = i\tau_1 E_{inc,x} + g_{rt,x} E_{circ,x} \quad (18)$$

For the x-component of the circulating field, the round trip attenuation coefficient is:

$$g_{rt,x} = \rho_1 \rho_2 e^{2ikL_{cavity}} e^{-i\phi} \quad (19)$$

Substituting equation (19) into (18) gives the following expression for the $E_{circ,x}$:

$$E_{circ,x} = \frac{i\tau_1}{1 - g_{rt,x}} E_{inc,x} \quad (20)$$

To find an expression for the x-component of the electric field just outside the second mirror, the phase of $E_{circ,x}$ in equation (20) is simply advanced by $e^{ikL_{cavity}} e^{-i\frac{\phi}{2}}$ and then multiplied by the transmission coefficient of the second mirror giving:

$$E_{trans,x} = \frac{-\tau_1 \tau_2 e^{ikL_{cavity}} e^{-i\frac{\phi}{2}}}{1 - g_{rt,x}} E_{inc,x} \quad (21)$$

The x-component of the normalized transmitted intensity is given by:

$$\frac{I_{trans,x}}{I_{inc,x}} = \frac{|E_{trans,x}|^2}{|E_{inc,x}|^2} \quad (22)$$

If the the reflectivity and the transmittance of the mirrors are defined by $R_1 = |\rho_1|^2$, $T_1 = |\tau_1|^2$, $R_2 = |\rho_2|^2$, $T_2 = |\tau_2|^2$, equations (21) and (22) can be combined to

given an expression for normalized transmitted intensity in terms of R_1, R_2, T_1 and T_2 :

$$T_x = \frac{T_1 T_2}{1 + R_1 R_2 - 2\sqrt{R_1 R_2} \cos(2kL_{cavity} - \phi)} \quad (23)$$

A similar treatment of the y-component of the fields yields:

$$T_y = \frac{T_1 T_2}{1 + R_1 R_2 - 2\sqrt{R_1 R_2} \cos(2kL_{cavity} + \phi)} \quad (24)$$

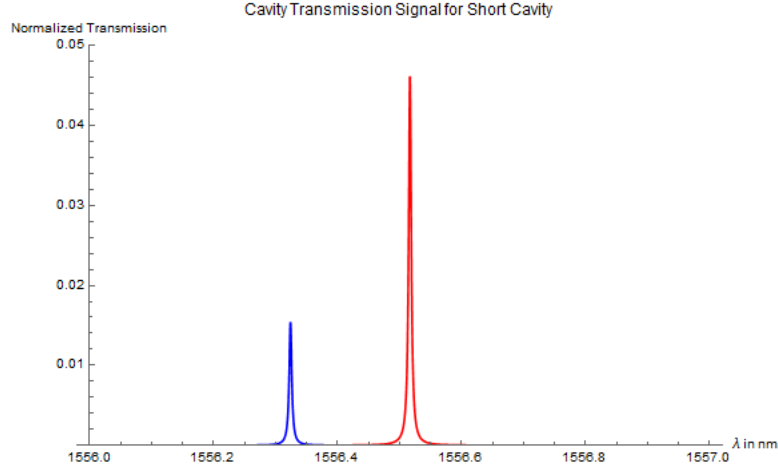


Figure 24: Plot of the calculated cavity transmission signal using the dielectric mirror reflectivity of 0.99984 and cavity length $L_{cavity} = 0.4mm$. As an example, incident light was assumed to be linearly polarized and oriented at 60° from the x-axis. For illustration purposes, a smaller “HCG reflectivity” (0.99 vs. 0.999 actual) and larger differential phase shift (0.4 vs. 0.02 actual) from the wave retarder were used in calculations.

Figures 24 and 25 show plots of the cavity transmission signal for two wavelength ranges - 1556nm-1557nm and 1550nm-1560nm. With the exception of the values used for the HCG reflectivity and the differential phase shift imparted by the wave retarder, all other quantities corresponded to those from short cavity experiments.

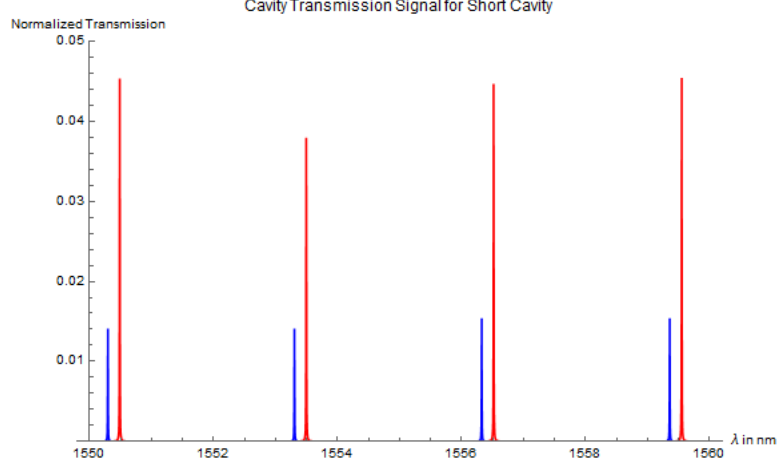


Figure 25: Similar to the plot in figure 24, but over a few FSR.

In order to fully account for the experimental data presented in chapter 3, the toy model needs to predict how the difference in phase shift imparted to the eigenmodes, how the orientation of the eigenmodes, and how the linewidth of the eigenmodes all change with wavelength. With regard to the first trend, the difference in phase shift imparted along the fast and slow axes is given by:

$$\phi_{slow} - \phi_{fast} = \frac{2\pi n_e t_{wave-retarder}}{\lambda_+} - \frac{2\pi n_o t_{wave-retarder}}{\lambda_-} \quad (25)$$

$$\phi_{slow} - \phi_{fast} \approx \left[\frac{2\pi t_{wave-retarder}}{\lambda} \right] (n_e - n_o) \quad (26)$$

If one assumes that $(n_e - n_o)$ is constant over the wavelength range from $1550nm$ to $1575nm$, which is reasonable given the small range involved, the toy model predicts that the difference in phase shift imparted to the polarization eigenmodes decreases with increasing wavelength. This is the opposite of what is observed in figure 18.

Therefore, the model fails to account for even the one trend it would seem well suited to explain.

4.1.2 RCWA Simulations

Stanford Stratified Structure Solver, or S^4 [23], a freely available simulation software that uses rigorous coupled wave analysis (RCWA), was used to examine the effect on HCG performance from a slight anisotropy in the refractive index of silicon nitride.

Anisotropy in the refractive index of low stress silicon nitride was treated as a small perturbation of the bulk refractive index. For computational simplicity, we assumed that the stressed silicon nitride films were uniaxial and that one of the ordinary axes was normal to the plane of the film. This is a reasonable simplification given the thickness of the HCGs ($t = 560nm$). Therefore, the orientation of the other ordinary axis and the extraordinary axis is described by a simple rotation with respect to the lattice vectors of the HCG's photonic crystal pattern (see figure 26).

The starting point for simulations was to find a combination of index perturbation and anisotropy rotation that fit experimental data at one particular wavelength. Since the HCG has its highest reflectivity at 1556nm, this wavelength was chosen as the starting anchor. Values for the index anisotropy in silicon nitride that best approximate experimental results at 1556nm are as follows - refractive indices along the fast and slow axes of 2.110 and 2.182, respectively, and a 41.5° rotation of the principal axes of anisotropy with respect to the unit vectors of the photonic crystal lattice (Λ_a, Λ_b).

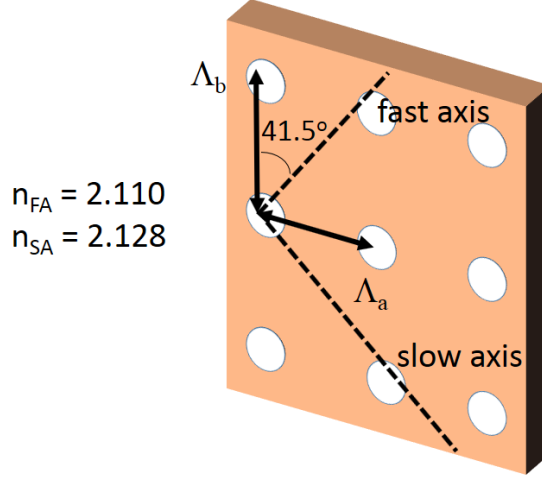


Figure 26: Model showing the relevant parameters used in simulations.

In order for a cavity formed from this HCG to sustain linearly polarized eigenmodes, there must be two polarizations of incident light for which the reflected light is linearly polarized at exactly the same angle. To determine the orientation of the eigenmodes, the difference between the orientation of the electric field vector for the incident field and the total field was calculated. The green portions in figure 27 show regions where there is almost no difference between the orientation of the electric field vectors of the incident field and the total field. There are only two values of incident polarization ($20^\circ, -70^\circ$) for which there is no difference between the orientation of the electric field vector for the incident field and the total field *over the entire propagation length* z . Naively, one would assume that the eigenmodes would be oriented along the principal axes of anisotropy. This was decidedly not the case. In fact, in order to obtain eigenmodes at $20^\circ, -70^\circ$ for a 0.018 perturbation in the permittivity, the principal axes of anisotropy need to be rotated by 41.5° with respect to the photonic crystal lattice vectors (Λ_a, Λ_b).

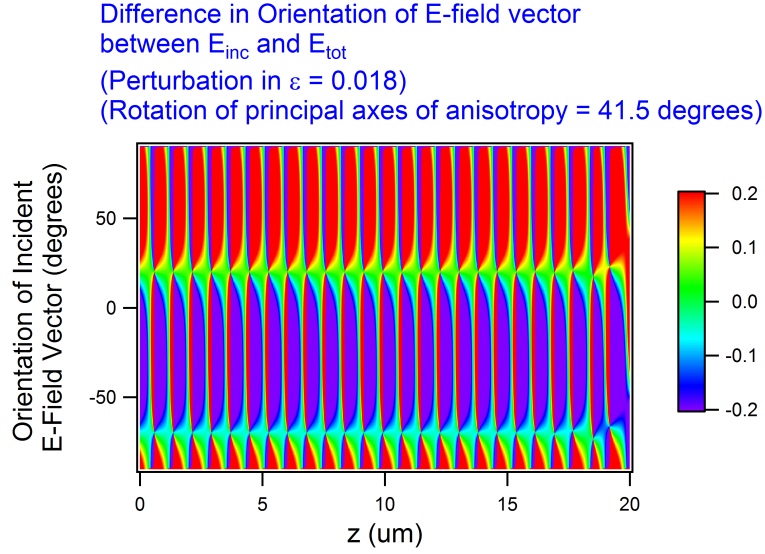


Figure 27: Graph of the difference in orientation between the electric field vector of the incident field ($\tan^{-1}(\frac{E_{yinc}}{E_{xinc}})$) and that of the total field ($\tan^{-1}(\frac{E_{ytot}}{E_{xtot}})$). The electric field was calculated for situations where an incident plane wave starts out at $z = 0\mu m$, propagates to the right, and encounters an HCG placed at $z = 20\mu m$. Green signifies regions where the orientation of the electric field vectors are nearly the same for both the incident ($E_{incident}$) and the total field ($E_{incident} + E_{reflected}$).

Once the eigenmodes were identified, the electric field profile of the reflected wave over the entire propagation length was determined for incident light whose electric field vectors coincide with the orientation of the eigenmodes, i.e., are oriented at -70° and 20° . The simulated results for the electric field of the reflected waves at each eigenmode orientation are shown in figures 28(a) and 28(b). Slices of the electric field at $x = 0\mu m$ in figures 28(a) and 28(b) are plotted together in figure 28(c). Sinusoidal fits to the two field profiles are used to determine the difference in phase shift imparted by the HCG to the two eigenmodes.

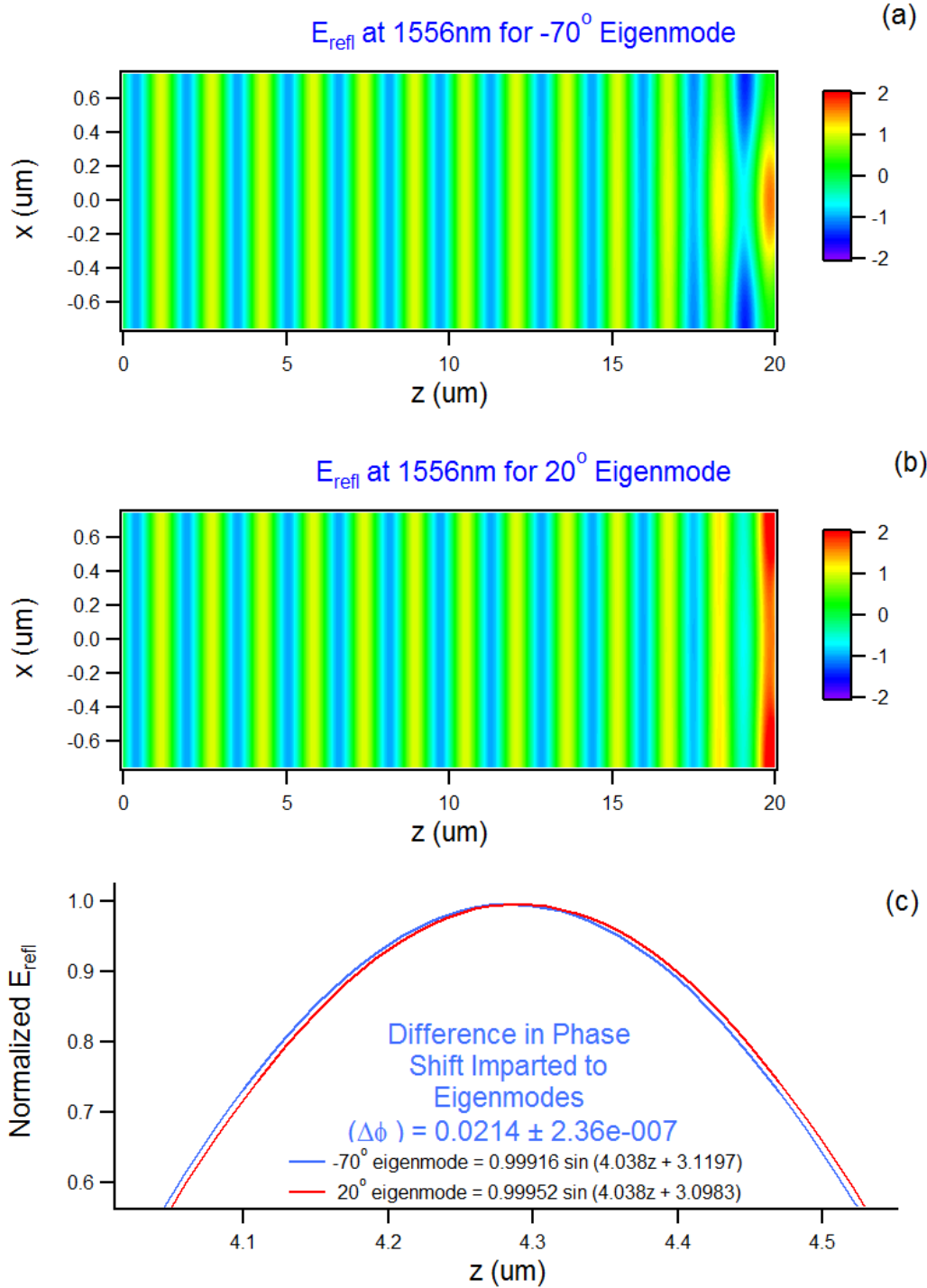


Figure 28: (a), (b) Magnitude of the electric field for the reflected waves, which propagate from right to left after encountering the HCG placed at $z = 20\mu m$. (c) Traces from (a) and (b) for $x = 0\mu m$.

The parameters for index anisotropy that fit experimental data at 1556nm were passed into simulations at other wavelengths in order to determine how the orientation of eigenmodes, the difference in phase shift imparted to eigenmodes, and the difference in reflectivity of eigenmodes all change with wavelength. Calculations similar to those laid out above were carried out for wavelengths at which there is recorded experimental data. A comparison of simulations and experimental results is presented in figures 29, 30, and 31.

With regard to the difference in phase shift imparted to eigenmodes, figure 29 shows that the trends from simulations match those in both the short cavity and the long cavity experiments.

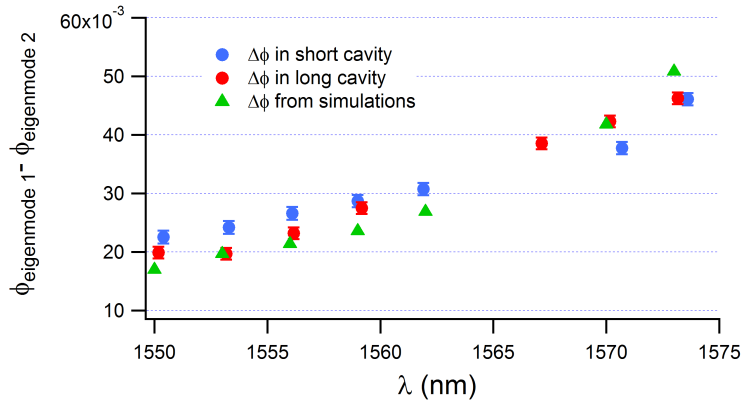


Figure 29: Comparison between the experimentally measured difference in phase shift imparted to orthogonal eigenmodes and the simulated difference in phase shift imparted to orthogonal eigenmodes.

Simulations also captured the fact that the orientation of eigenmodes changes with wavelength. Moreover, just like experimental data, the change in the orientation of eigenmodes levels off at around 1553nm and increases linearly with wavelength from 1556nm to 1573nm .

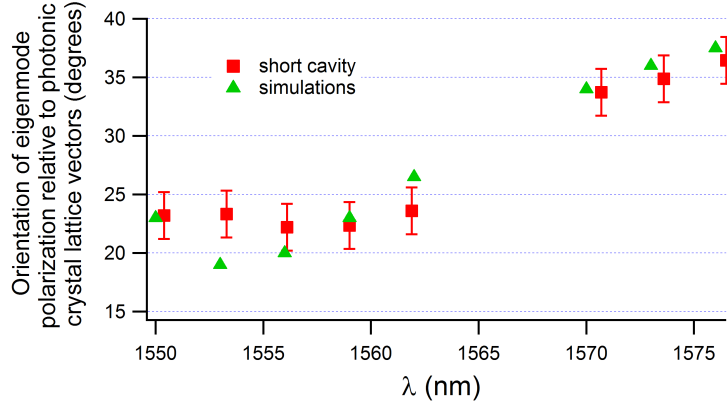


Figure 30: Change in the orientation of the electric field vector of eigenmodes as a function of wavelength.

Finally, figure 31 compares simulated reflectivity for each eigenmode with the corresponding results from short cavity experiments. The trends in simulations match those seen in the experimental data although the results diverge at longer wavelengths.

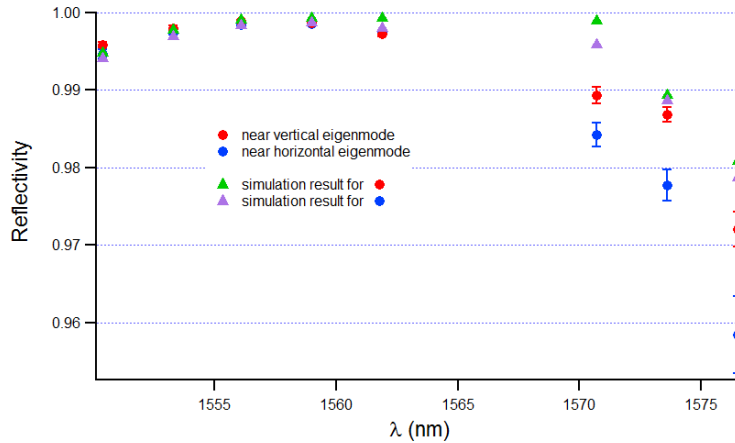


Figure 31: Change in the reflectivity of the HCG for the orthogonal eigenmodes.

The reasons for this divergence may partly be explained by the so-called “anomalous peak” in figure 20. One deficiency of our simulations is that the excitation field was assumed to be an infinite plane wave at normal incidence. However, any real beam will have a finite spot size and the plane wave decomposition of such a beam

will include off-normal components. As Foley et al. [14] have shown, plane waves incident at oblique angles can give rise to narrowband transmission features just like the one seen in figure 20. Therefore, we believe it is reasonable to expect some deviation between experimental results and simulations based on a single plane wave incident at 90° , especially in the vicinity of the “anomalous peak.”

Although simulations replicate all the trends seen in experimental data, numerical agreement is certainly not perfect. When one considers that simulations predict the unique and unexpected trends observed in cavity experiments, it undoubtedly suggests that index anisotropy holds at least some of the answer to why 2D HCGs based on symmetric photonic crystal lattices are sensitive to the polarization of incident light.

4.2 Separation of Absorption from Scattering

The coefficient of finesse is an important measure of cavity performance from the standpoint of optomechanics. The higher the finesse, the greater the build up of optical power circulating in the cavity and, therefore, the greater the force exerted by radiation pressure on a moveable end mirror. Moreover, to achieve sideband cooling of an optomechanical element, the linewidth of a cavity resonance, which is related to the finesse, needs to be much smaller than the vibrational frequency of the moveable mirror. Given the ready availability of high reflectivity dielectric mirrors, the performance of Fabry-Pérot cavities formed from a dielectric mirror and an HCG will likely be limited by the reflectivity of the HCG.

When $1 - R_{HCG} \gg 1 - R_{dielectric}$, equation (5) simplifies to:

$$F = \frac{2\pi}{(1 - R_{HCG})} \quad (27)$$

Equating this expression for the finesse to that in equation (2) gives a relationship between the linewidth of a cavity resonance and the reflectivity of the HCG at a particular frequency.

$$\Delta\nu_{opt} = \left[\frac{2\pi}{FSR} \right] (1 - R_{HCG}) \quad (28)$$

As the reflectivity of the HCG approaches unity, small increases in HCG reflectivity lead to larger and larger gains in cavity finesse (or shorter and shorter resonance linewidths). For example, increasing HCG reflectivity from 97.5% to 99.5% results in a fivefold reduction in the resonance linewidth. However, an increase in HCG reflectivity from 99.5% to 99.9%, a smaller absolute improvement, results in the same fivefold reduction in resonance linewidth. Given the potential for large improvements in performance as $R_{HCG} \rightarrow 1$, it is critical to understand how different mechanisms contribute to the optical losses in this regime. For example, if scattering is the dominant source of loss, it can possibly be mitigated by refinement of the fabrication process. Likewise, high absorption would weigh in favor of moving to a lower loss material system like stoichiometric Si_3N_4 .

4.2.1 Effect of Absorption Loss on HCG Reflectivity

Simulations were carried out for two device designs. The parameters for the first, a broadband reflector, were based on the geometry of fabricated devices presented

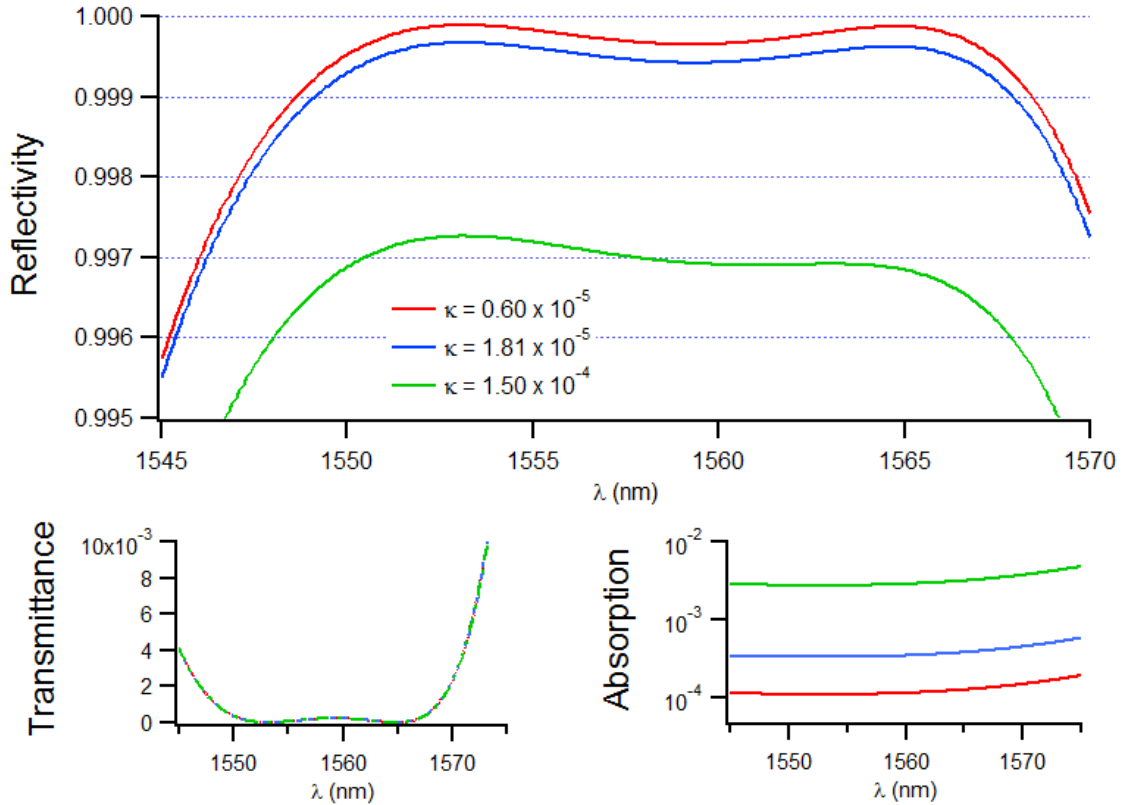


Figure 32: Change in reflectivity, transmittance, and the normalized absorption loss for a broadband reflector. (Device parameters: $\Lambda a = \Lambda b = 1.508 \mu m$, hole radius = $0.569 \mu m$, thickness = $560 nm$, $n = 2.11$)

in earlier chapters. The latter device was designed to function as a high Q reflector. Figures 32 and 33 show the results of simulations for three different values of the imaginary part of the refractive index κ . These values of κ were drawn from literature and primarily chosen for illustration purposes. The highest value, 1.5×10^{-4} , is taken from Jayich [7], which measured κ for a commercially available $50 nm$ SiN x-ray window. The middle value, 1.81×10^{-5} , is the average of the upper and lower bounds on κ obtained from measurements of low stress silicon nitride films grown at the National Institute of Standards and Technology's (NIST) nanofabrication facility [24]. The lowest value used in these simulations is taken from results reported in Wilson

[16], which are for stoichiometric silicon nitride.

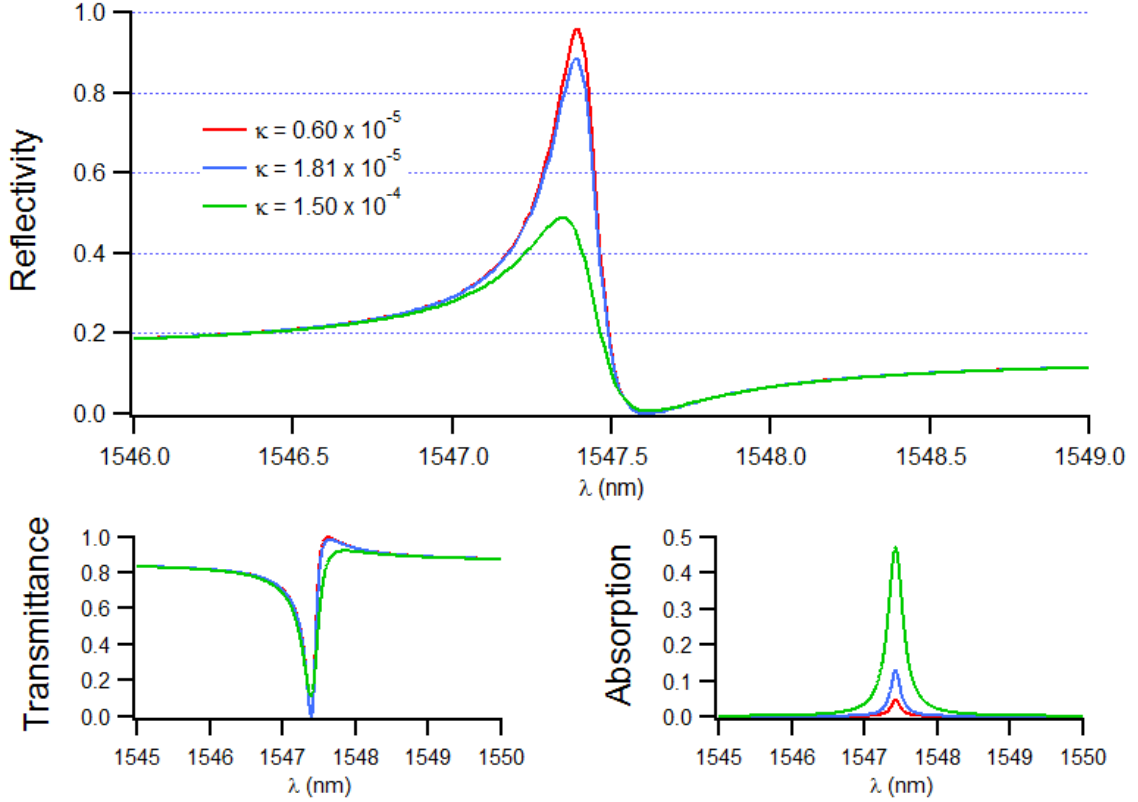


Figure 33: Change in reflectivity, transmittance, and the normalized absorption loss for a high Q reflector. (Device parameters: $\Lambda a = \Lambda b = 1.310\mu m$, hole radius = $0.131\mu m$, thickness = $321.4nm$, $n = 1.943$)

These results suggest that increased absorption comes almost entirely at the expense of the reflectivity. In the case of the high Q reflector, the decrease in peak reflectivity is also accompanied by a drop in the optical Q .

4.2.2 Estimate of Scattering Losses

The previous chapter presented results from cavity experiments that determined the reflectivity (R_{HCG}) and the transmittance (T_{HCG}) of an HCG, as well as a term 2Γ that captured the sum all scattering and absorption losses per round trip in the

cavity. 2Γ is defined as being equal to the sum ($2\gamma_{dielectric} + 2\gamma_{HCG}$). While one could go to the trouble of first determining $2\gamma_{dielectric}$ and then using that value to find $2\gamma_{HCG}$, one could also simply estimate $2\gamma_{HCG}$ from the relation $1 - R_{HCG} - T_{HCG}$.

The data from figure 31 can be presented in terms of the sum of all optical losses ($1 - R$), thereby allowing one visualize how this quantity changes with wavelength. What stands out in this figure is the disagreement between simulations and experiment for wavelengths ranging from 1559nm to 1570nm. This disagreement, in and of itself, is not necessarily troubling. After all, the data may simply reflect the presence of scattering losses in this wavelength range. Rather, what is concern is that this disagreement occurs in the in the vicinity of the so-called “anomalous peak” identified in figure 20. Since our simulations assumed that incident field is an infinite plane wave normal to the surface of the HCG, they do not capture the increased transmission between 1562nm and 1570nm, as shown in figure 20. This is in clear contrast to the graph in the bottom left corner of figure 32, which represents the response of simulated data. Therefore, comparing data from cavity measurements with those from simulations will result in improperly attributing transmission losses to those due to scattering.

The divergence between simulation and experiment is much less pronounced for the “near horizontal” eigenmode. Consequently, it may be possible to extract some useful information about scattering losses by comparing cavity measurements to results from simulations. Figure 35 plots two quantities for both experimental data and simulation results. At the shorter wavelengths, there is good agreement between the $(1 - R)$ values in both cases. Unsurprisingly, this changes in the vicinity of the

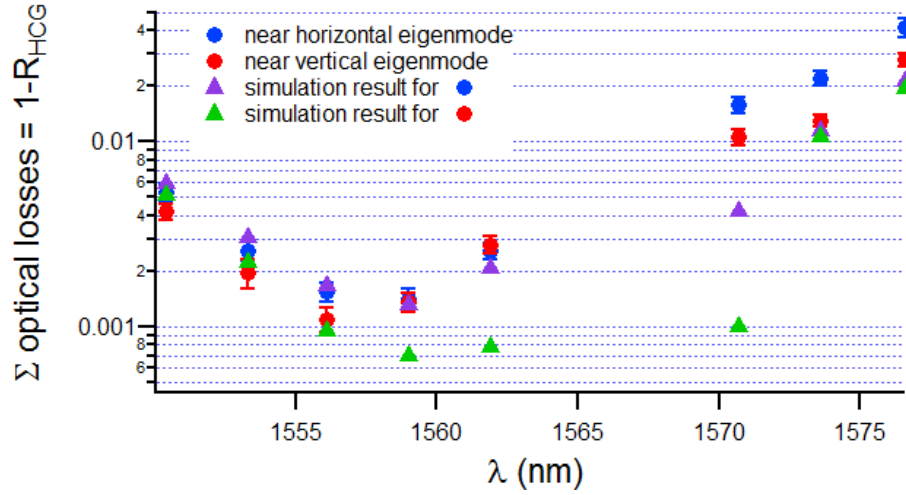


Figure 34: Comparison of Σ optical losses from experiments with those from simulations.

“anomalous peak” where a much lower reflectivity is suggested by cavity experiments.

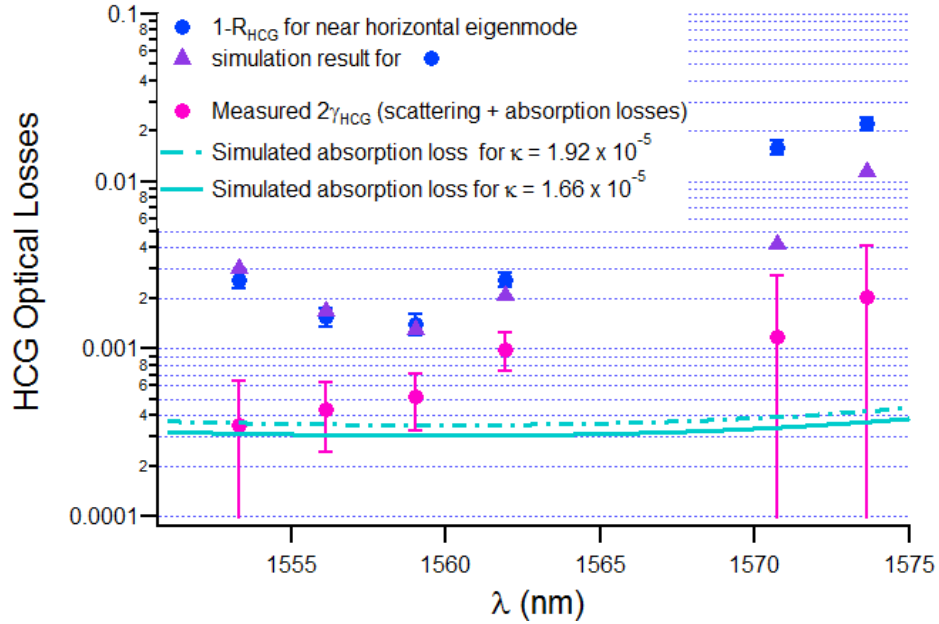


Figure 35: Comparison of different components of the optical loss in HCGs for the near horizontal eigenmode.

Figure 35 also plots the value of $2\gamma_{\text{HCG}}$ and the simulated absorption losses for two different values of the imaginary part of the refractive index κ . These values

correspond to the upper and lower limits on κ determined in reference [24] for low stress silicon nitride membranes in the telecom band. Increases in the total optical loss determined from experiments at 1559nm and 1562nm appear to coincide with a commensurate increase in $2\gamma_{HCG}$. Since losses from absorption are expected to be constant over much of this wavelength range, the upticks in $2\gamma_{HCG}$ can possibly be attributed to an increase in scattering losses. However, without accounting for the effect of finite beam size and, therefore, the effect of off-normal plane wave components, we cannot make any definitive statements about the loss due to scattering off the HCG.

4.3 Summary

RCWA simulations in which a slight anisotropy was introduced into the refractive index silicon nitride were shown to track with experimental results. In particular, the simulations fully captured various trends in the behavior of polarization eigenmodes as a function of wavelength. The quality of the agreement between simulation and experiment opens up the possibility of using HCGs to measure both the magnitude and orientation of index anisotropy in thin film dielectric materials.

However, this success did not carry over to efforts to distinguish between scattering and absorption losses. In contrast to real beams, which have a finite size and include off-normal plane wave components, our simulations only considered the response of HCGs to infinite plane waves at normal incidence. Consequently, the appearance of narrowband transmission peaks within the high reflectivity region was missed by simulations. Unfortunately, our approach to separating absorption from scattering

losses hinged on good agreement between experiments and simulations because the estimate for scattering losses is obtained by subtracting simulated absorption loss from the measured total loss $2\gamma_{HCG}$.

Chapter 5 Conclusions and Future Work

5.1 Conclusions

The overall goal of this thesis is to examine how the optical properties of stressed silicon nitride films affect the performance of high contrast gratings. In particular, we looked at the performance of two types of 2D HCG designs – polarization insensitive, broadband reflectors and narrowband transmission filters.

2D HCGs based on symmetric photonic crystal patterns are expected to be insensitive to the polarization of light at normal incidence. Results from cavity experiments showed that these HCGs, which were fabricated on low stress silicon nitride membranes, exhibited polarization-dependent behavior. In Fabry-Pérot cavities that used these HCGs as one of the end mirrors, the sensitivity to polarization manifested as the breaking of degeneracy between polarization eigenmodes. We initially looked to an intuitive toy model to introduce the phase shifts referenced in (14). This simple model for membrane birefringence could not account for the results of experiments. In particular, it could not explain following trends - the change in orientation of eigenmodes, the change in eigenmode separation, or the difference in linewidths for orthogonal eigenmodes - all as a function of wavelength. However, RCWA simulations in which a small anisotropy was introduced into the refractive index of silicon nitride replicated all these unexpected trends. Simulated parameters that best fit experimental data suggested that our low stress silicon nitride films have refractive indices of $n_o = 2.11$ and $n_e = 2.13$, as well as principal axes of anisotropy that are rotated with respect to the photonic crystal lattice by 41.5° .

The observed anisotropy in the refractive index of silicon nitride has implications for the use of 2D HCGs in optomechanics experiments. One goal of our work is to use HCGs as an end mirror in a laser cavity. The hope is to demonstrate a laser capable of optically cooling one of its end mirrors. Breaking the degeneracy between polarization eigenmodes could result in a laser that hops from one polarization eigenmode to the other and back, thus complicating efforts to achieve optical cooling of the HCG. Until one finds a way to reduce the anisotropy in silicon nitride films, 2D HCGs should be designed to function as polarizing reflectors.

This thesis also sought to determine the contributions of different mechanisms to optical losses in HCGs. When an HCG and a known reference mirror are used to form a Fabry-Pérot cavity, the sum of all optical losses due to the HCG can be determined from the linewidth of the cavity transmission signal. We showed that it is possible to separate transmission losses from the sum of scattering and absorption losses by using information from the cavity reflection signal. Although scattering and absorption losses could not be separated from one another through cavity experiments, we used simulations to estimate the expected loss due to absorption. The hope was to extract an estimate for scattering losses by comparing the simulated absorption losses with measurements of $2\gamma_{HCG}$ - the total absorption and scattering loss due to the HCG. However, due to the large discrepancies between theory and experiment at longer wavelengths, we do not believe it is prudent to arrive at an estimate for scattering based on this approach. We believe our simulations need to account for off-normal plane wave components before scattering losses can be determined by simply subtracting simulated absorption losses from measured values of $2\gamma_{HCG}$.

5.2 Future Work

5.2.1 Design and Fabrication

A natural extension of the work presented in this thesis is to fabricate HCGs on stoichiometric silicon nitride. In addition to increasing their frequency of vibration, it should also be possible to increase the reflectivity of HCGs.

Our efforts to estimate the scattering loss suffered from one major drawback - an inability to fit experimental data to simulations of the reflectivity and optical losses at all wavelengths. Our simulations assumed that the incident field was an infinite plane wave. However, the plane wave decomposition of a Gaussian beam includes off-normal components. When simulations of the broadband reflector described in the previous chapter are run for off-normal plane wave components, we find that there is a small narrowband transmission peak around 1566nm, just as was observed in figure 20. Fully accounting for off-normal plane wave components may make it possible to obtain a better fit between experiment and simulation, thereby allowing one to use simulated absorption losses to arrive at an estimate for loss due to scattering.

Conversely, by accounting for the effect of off-normal plane wave components at the design stage, it is possible to find regions of parameter space where the response of the HCG is largely unaffected by finite beam size. Our most recent set of devices (see figure 36) were based on such a design and, at first glance, does not appear to exhibit any narrowband transmission features within the high reflectivity region.

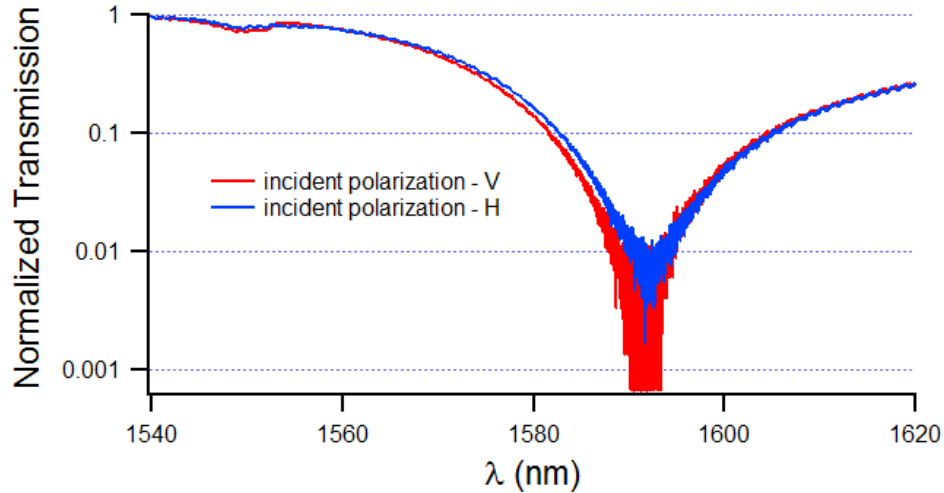


Figure 36: Normalized transmission of a focused beam through a new 2D HCG that was fabricated from stoichiometric Si_3N_4 .

5.2.2 Metrology

The ability of simulations to replicate the trends in eigenmode behavior with respect to wavelength point to the possibility of using HCGs to detect a slight anisotropy in the refractive index of thin dielectric films. Our analysis from chapter 4 suggests that it should be possible to determine not only the magnitude, but also the orientation of the principal axes of anisotropy.

5.2.3 Optomechanics

A recent paper by Buters [25] suggests one potential application for the broadband HCGs examined in this thesis. In particular, they considered a situation where the separation between eigenmodes in a polarization nondegenerate Fabry-Pérot cavity is equal to twice the mechanical frequency of the moveable mirror. When a probe is detuned such that its frequency is exactly between two orthogonal polarization

eigenmodes, one can then use polarization as a knob to switch between cooling or self oscillation of the moveable mirror. Buters et al. were limited by the fact that they used an astigmatic dielectric mirror to create their polarization nondegenerate cavity. Consequently, they had only a limited ability to tune the separation between eigenmodes. As our results in figure 13 show, changing the separation between eigenmodes over a few MHz is a simple matter of changing the excitation wavelength by a small amount.

Appendix A: Relating mirror parameters to the transmitted and reflected signals

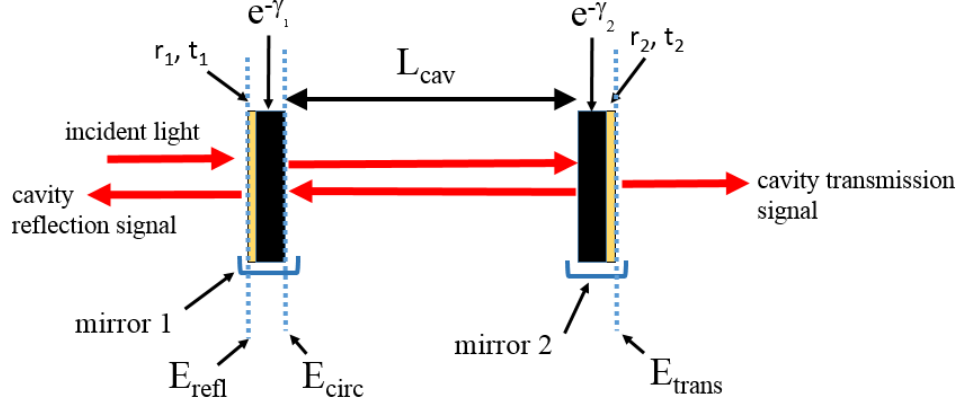


Figure 37: Toy model of a Fabry-Pérot cavity. Each mirror is modeled as a compound element comprising a lossy medium and a lossless reflector ($T + R = 1$). On each pass through the lossy medium, the amplitude of the electric field is attenuated by factors of $e^{-\gamma_1}$ and $e^{-\gamma_2}$ at mirrors 1 and 2, respectively. The dashed lines indicate the planes at which the reflected, circulating, and transmitted fields are calculated.

Definitions

For the Fabry-Pérot cavity of length L_{cav} above, let the reflection and transmission coefficients of the two lossless reflectors be given by r_1, it_1, r_2, it_2 . These coefficients are related to the respective reflectivities ($R_1 = |r_1|^2$, $R_2 = |r_2|^2$) and transmittances ($T_1 = |it_1|^2$, $T_2 = |it_2|^2$). Note that for the lossless reflector,

$$r_1^2 = \sqrt{1 - t_1^2} \quad (29)$$

$$r_2^2 = \sqrt{1 - t_2^2} \quad (30)$$

The passive optical losses at each mirror can be defined with respect to $e^{-\gamma_i}$, which represents the factor by which the amplitude of the electric field is attenuated per pass through the lossy medium. Therefore, the amplitude of the electric field is attenuated by a factor of $e^{-2\gamma_i}$ after each reflection.

Circulating field

The round trip attenuation coefficient g_{rt} of the cavity is given by

$$g_{rt} = r_1 r_2 e^{2ikL_{cav}} e^{-2i(\gamma_1 + \gamma_2)} \quad (31)$$

The electric field of the circulating power (just in front of the first mirror) is the sum of two contributions - incident light that couples into the cavity through mirror 1 and the attenuated circulating power after one round trip through the cavity. In the steady state,

$$E_{circ} = it_1 E_{inc} + g_{rt} E_{circ} \quad (32)$$

The normalized electric field of the circulating power just in front of the first mirror is

$$\frac{E_{circ}}{E_{inc}} = \frac{it_1 e^{-\gamma_1}}{1 - g_{rt}} \quad (33)$$

Transmitted field

To find the normalized electric field of the transmitted signal just outside the second mirror, advance the phase of E_{circ} by $e^{ikL_{cav}}$ and then multiply the result by $ie^{-\gamma_2}t_2$ to account for transmission through mirror 2

$$\frac{E_{trans}}{E_{inc}} = \frac{-t_1 t_2 e^{-(\gamma_1 + \gamma_2)} e^{ikL_{cav}}}{1 - r_1 r_2 e^{-2(\gamma_1 + \gamma_2)} e^{2ikL_{cav}}} \quad (34)$$

Let us define $\Gamma = (\gamma_1 + \gamma_2)$. Therefore, Γ represents fractional amplitude of the electric field after one pass through both lossy mediums.

Equation (34) can now be rewritten as

$$\frac{E_{trans}}{E_{inc}} = \frac{-t_1 t_2 e^{-\Gamma} e^{ikL_{cav}}}{1 - r_1 r_2 e^{-2\Gamma} e^{2ikL_{cav}}} \quad (35)$$

The accumulated phase kL_{cav} can be expressed in terms of the frequency of the wave,

$$kL_{cav} = \frac{2\pi}{\lambda} L_{cav} = \frac{2\pi\nu}{c} L_{cav} \quad (36)$$

However, the free spectral range (ν_{FSR}) of a Fabry-Pérot cavity is nothing but $\frac{c}{2L_{cav}}$. The accumulated phase can now be rewritten as

$$kL_{cav} = \frac{\pi\nu}{\nu_{FSR}} \quad (37)$$

Recall that any arbitrary frequency ν can be expressed in terms of a detuning $\delta\nu$

from the free spectral range (ν_{FSR})

$$\nu = N\nu_{FSR} + \delta\nu \quad (38)$$

where N is a natural number. Since N is a natural number, $e^{ikL_{cav}}$ and $e^{2ikL_{cav}}$ simplify to

$$e^{ikL_{cav}} = (-1)^N e^{\frac{i\pi\delta\nu}{\nu_{FSR}}} \quad (39)$$

$$e^{2ikL_{cav}} = e^{\frac{2i\pi\delta\nu}{\nu_{FSR}}} \quad (40)$$

Substituting (39) and (40) into (34) gives the transmission coefficient of the cavity t_{cav} .

$$t_{cav} = (-1)^N \frac{-t_1 t_2 e^{-\frac{\Gamma}{2}} e^{\frac{i\pi\delta\nu}{\nu_{FSR}}}}{1 - r_1 r_2 e^{-\Gamma} e^{\frac{2i\pi\delta\nu}{\nu_{FSR}}}} \quad (41)$$

The transmittance of the cavity T_{cav} is simply $|t_{cav} * t_{cav}^*|$. By completing the square for the term in the denominator and using the half angle formula, T_{cav} can be written as:

$$T_{cav} = \frac{T_1 T_2 e^{-\Gamma}}{(1 - r_1 r_2 e^{-\Gamma})^2 + r_1 r_2 e^{-\Gamma} 4 \sin^2\left(\frac{\pi\delta\nu}{\nu_{FSR}}\right)} \quad (42)$$

However, in equations (29) and (30), we defined $r_1^2 = \sqrt{1 - T_1}$ and $r_2^2 = \sqrt{1 - T_2}$. For a high finesse cavity, which features mirrors with low transmittance and low loss,

$1 - r_1 r_2 e^{-\Gamma}$ simplifies to

$$1 - r_1 r_2 e^{-\Gamma} = 1 - \sqrt{1 - T_1} \sqrt{1 - T_2} (1 - \Gamma) \quad (43)$$

$$1 - r_1 r_2 e^{-\Gamma} \approx 1 - \left(1 - \frac{T_1}{2}\right) \left(1 - \frac{T_2}{2}\right) (1 - \Gamma) \quad (44)$$

Collecting only the lowest order terms gives

$$1 - r_1 r_2 e^{-\Gamma} \approx \frac{1}{2}(T_1 + T_2 + \Gamma) \quad (45)$$

This term is nothing but half times the round trip optical losses and will be denoted by ϵ . Using this relation for ϵ in equation (42) and noticing that r_1 , r_2 , and $e^{-\Gamma}$ for a low loss cavity all approach unity, we get

$$T_{cav} = \frac{T_1 T_2}{\epsilon^2 + 4 \sin^2\left(\frac{\pi \delta \nu}{\nu_{FSR}}\right)} \quad (46)$$

But the cavity finesse F is given by 2π divided by the sum of all optical losses, or 2ϵ . Therefore, $\epsilon = \frac{\pi}{F}$. At resonance, the cavity detuning $\delta \nu$ is zero and T_{cav} reduces to

$$T_{cav} = \left(\frac{F}{\pi}\right)^2 T_1 T_2 \quad (47)$$

which is nothing but the maximum of the normalized transmission signal of the cavity.

Reflected field

The reflected field is the sum of two contributions - the promptly reflected beam off mirror 1 and the fraction of the circulating power that is transmitted through mirror 1 (to get this value, advance E_{circ} (from just to the right of the first mirror all the way to the second mirror and back and then multiply by $ie^{-\gamma_1}t_1$ to account for transmission through mirror 1).

$$E_{refl} = r_1 E_{inc} + it_1 r_2 e^{2ikL_{cav}} e^{-i(\gamma_1+2\gamma_2)} E_{circ} \quad (48)$$

The normalized electric field of the reflected wave is given by

$$\frac{E_{refl}}{E_{inc}} = r_1 + \left(\frac{E_{circ}}{E_{inc}} \right) (it_1 r_2 e^{2ikL_{cav}} e^{-i(\gamma_1+2\gamma_2)}) \quad (49)$$

Using the result from equation (33),

$$\frac{E_{refl}}{E_{inc}} = r_1 - \frac{t_1^2 e^{-\Gamma} e^{2ikL_{cav}}}{1 - r_1 r_2 e^{-\Gamma} e^{2ikL_{cav}}} \quad (50)$$

Using $t_1^2 = 1 - r_1^2$ for the lossless reflector of the toy model gives the following expression for the reflection coefficient of the cavity r_{cav}

$$r_{cav} = \frac{r_1^2 - r_1 r_2 e^{-\Gamma} e^{2ikL_{cav}}}{1 - r_1 r_2 e^{-\Gamma} e^{2ikL_{cav}}} \quad (51)$$

Factoring r_1 from the numerator leaves the term $r_1 - r_2 e^{-\Gamma}$, which we now denote as ξ . We can simplify this term further in a manner similar what was done in (43).

After collecting only the lowest order terms we have

$$r_1 - r_2 e^{-\Gamma} \approx \frac{1}{2}(-T_1 + T_2 + \Gamma) \quad (52)$$

After incorporating the definitions for ϵ , $e^{2ikL_{cav}}$ (equation (40)), and ξ into equation (51), we can obtain an expression for the reflectivity of the cavity $|r_{cav} * r_{cav}^*|$, which is nothing but R_{cav} . By completing the square for the terms in the numerator and the denominator and then using the half angle formula, R_{cav} can be written as

$$R_{cav} = \frac{\xi^2 + 4r_1 r_2 e^{-\Gamma} \sin^2\left(\frac{\pi\delta\nu}{\nu_{FSR}}\right)}{\epsilon^2 + 4r_1 r_2 \sin^2\left(\frac{\pi\delta\nu}{\nu_{FSR}}\right)} \quad (53)$$

For a low loss cavity, r_1 , r_2 , and $e^{-\Gamma}$ all approach unity, giving

$$R_{cav} = \frac{\xi^2 + 4\sin^2\left(\frac{\pi\delta\nu}{\nu_{FSR}}\right)}{\epsilon^2 + 4\sin^2\left(\frac{\pi\delta\nu}{\nu_{FSR}}\right)} \quad (54)$$

As noted earlier, $\epsilon = \frac{\pi}{F}$ and $\xi = r_1 - r_2 e^{-\Gamma} \approx \frac{1}{2}(-T_1 + T_2 + \Gamma)$. Therefore, at resonance (cavity detuning $\delta\nu = 0$) R_{cav} simplifies to R_{cav} simplifies to

$$R_{cav} = \left(\frac{F}{2\pi}\right)^2 (-T_1 + T_2 + 2\Gamma)^2 \quad (55)$$

which is nothing but the minimum of the normalized reflection signal of the cavity.

Bibliography

- [1] Alexander G. Krause, Martin Winger, Tim D. Blasius, Qiang Lin, and Oskar Painter. A high-resolution microchip optomechanical accelerometer. *Nature Photonics*, 6(11):768–772, November 2012.
- [2] D. E. Chang, A. H. Safavi-Naeini, M. Hafezi, and O. Painter. Slowing and stopping light using an optomechanical crystal array. *New Journal of Physics*, 13(2):023003, 2011.
- [3] Gregory M. Harry and the LIGO Scientific Collaboration. Advanced LIGO: the next generation of gravitational wave detectors. *Classical and Quantum Gravity*, 27(8):084006, 2010.
- [4] T. J. Kippenberg and K. J. Vahala. Cavity Opto-Mechanics. *Optics Express*, 15(25):17172–17205, December 2007.
- [5] Markus Aspelmeyer, Tobias J. Kippenberg, and Florian Marquardt. Cavity optomechanics. *Reviews of Modern Physics*, 86(4):1391–1452, December 2014.
- [6] Michael Metcalfe. Applications of cavity optomechanics. *Applied Physics Reviews*, 1(3):031105, September 2014.
- [7] A. M. Jayich, J. C. Sankey, B. M. Zwickl, C. Yang, J. D. Thompson, S. M. Girvin, A. A. Clerk, F. Marquardt, and J. G. E. Harris. Dispersive optomechanics: a membrane inside a cavity. *New Journal of Physics*, 10(9):095008, 2008.
- [8] H. R. Böhm, S. Gigan, F. Blaser, A. Zeilinger, M. Aspelmeyer, G. Langer, D. Bäuerle, J. B. Hertzberg, and K. C. Schwab. High reflectivity high-Q micro-mechanical Bragg mirror. *Applied Physics Letters*, 89(22):223101, November 2006.
- [9] Dustin Kleckner, William Marshall, Michiel J. A. de Dood, Khodadad Nima Dinyari, Bart-Jan Pors, William T. M. Irvine, and Dirk Bouwmeester. High Finesse Opto-Mechanical Cavity with a Movable Thirty-Micron-Size Mirror. *Physical Review Letters*, 96(17):173901, May 2006.
- [10] I. Tittonen, G. Breitenbach, T. Kalkbrenner, T. Müller, R. Conradt, S. Schiller, E. Steinsland, N. Blanc, and N. F. de Rooij. Interferometric measurements of the position of a macroscopic body: Towards observation of quantum limits. *Physical Review A*, 59(2):1038–1044, February 1999.
- [11] Steven G. Johnson, Shanhui Fan, Pierre R. Villeneuve, J. D. Joannopoulos, and L. A. Kolodziejski. Guided modes in photonic crystal slabs. *Physical Review B*, 60(8):5751–5758, August 1999.

- [12] Onur Kilic, Sora Kim, Wonjoo Suh, Yves-Alain Peter, Aasmund S. Sudbø, Mehmet F. Yanik, Shanhui Fan, and Olav Solgaard. Photonic crystal slabs demonstrating strong broadband suppression of transmission in the presence of disorders. *Optics Letters*, 29(23):2782, December 2004.
- [13] Connie J. Chang-Hasnain and Weijian Yang. High-contrast gratings for integrated optoelectronics. *Advances in Optics and Photonics*, 4(3):379, September 2012.
- [14] J. M. Foley, S. M. Young, and J. D. Phillips. Symmetry-protected mode coupling near normal incidence for narrow-band transmission filtering in a dielectric grating. *Physical Review B*, 89(16):165111, April 2014.
- [15] High quality mechanical and optical properties of commercial silicon nitride membranes. *Applied Physics Letters*, 92(10):103125, March 2008.
- [16] D. J. Wilson, C. A. Regal, S. B. Papp, and H. J. Kimble. Cavity Optomechanics with Stoichiometric SiN Films. *Physical Review Letters*, 103(20):207204, November 2009.
- [17] Utku Kemiktarak, Michael Metcalfe, Mathieu Durand, and John Lawall. Mechanically compliant grating reflectors for optomechanics. *Applied Physics Letters*, 100(6):061124, February 2012.
- [18] Utku Kemiktarak, Mathieu Durand, Michael Metcalfe, and John Lawall. Cavity optomechanics with sub-wavelength grating mirrors. *New Journal of Physics*, 14(12):125010, 2012.
- [19] Onur Kilic, Shanhui Fan, and Olav Solgaard. Analysis of guided-resonance-based polarization beam splitting in photonic crystal slabs. *JOSA A*, 25(11):2680–2692, November 2008.
- [20] Jeongwon Lee, Bo Zhen, Song-Liang Chua, Wenjun Qiu, John D. Joannopoulos, Marin Soljačić, and Ofer Shapira. Observation and Differentiation of Unique High-Q Optical Resonances Near Zero Wave Vector in Macroscopic Photonic Crystal Slabs. *Physical Review Letters*, 109(6):067401, August 2012.
- [21] A.E. Siegman. *Lasers*. University Science Books, 1986.
- [22] Eric D. Black. An introduction to Pound–Drever–Hall laser frequency stabilization. *American Journal of Physics*, 69(1):79–87, December 2000.
- [23] Victor Liu and Shanhui Fan. S4: A free electromagnetic solver for layered periodic structures. *Computer Physics Communications*, 183(10):2233–2244, 2012.
- [24] Corey Stambaugh, Mathieu Durand, Utku Kemiktarak, and John Lawall. Cavity-enhanced measurements for determining dielectric-membrane thickness and complex index of refraction. *Applied Optics*, 53(22):4930–4938, August 2014.

- [25] F. M. Buters, M. J. Weaver, H. J. Eerkens, K. Heck, S. de Man, and D. Bouwmeester. Optomechanics with a polarization nondegenerate cavity. *Physical Review A*, 94(6):063813, December 2016.